

Report LR-796

Experimental and Computational Study of a Blunt Cylinder-Flare Model in High Supersonic Flow

October 1995

E.M. Houtman / W.J. Bannink / B.H. Timmerman

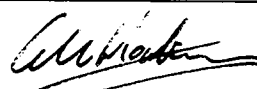
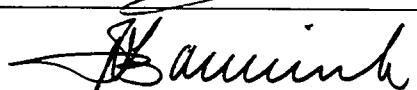
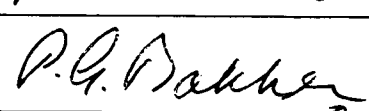

Experimental and Computational Study of a Blunt Cylinder-Flare Model in High Supersonic Flow

E.M. Houtman / W.J. Bannink / B.H. Timmerman

Organization : TUD/LR/A1-HSA
Document code : LR - 796

Date : October 1995
Page : i

Title	: Experimental and Computational Study of a Blunt-Cylinder-Flare Model in High-Supersonic Flow
Author(s)	: E.M. Houtman, W.J. Bannink and B.H. Timmerman
Abstract	: The high supersonic flow around a generic re-entry body (hemispherical-nose-cylinder with conical flare) at incidence has been investigated experimentally and numerically. Visualization studies using short exposure shadowgraphy and surface oil-flow have provided a qualitative understanding of the flow physics. Quantitative results are obtained with a holographic interferometry system with digital image processing. These results are compared with post-processed numerical data from inviscid flow simulations with a 3D Euler code. Extensive surface pressure measurements deliver a detailed pressure distribution on the body which can be used as a validation of computational codes. Interesting features of the flow are a complex surface flow topology at the leeward side with various separations, and a shock-shock interaction in the windward region interfering with the body.
Keyword(s)	: Euler method, interferometry, high-supersonic flows, shock-shock interactions

Date	October 1995
Prepared	E.M. Houtman 
Verified	W.J. Bannink 
Approved	P.G. Bakker 
Authorized EB	P.G. Bakker 

Acknowledgements

The authors wish to express their gratitude to the following students who contributed to this investigation: Mr. P.A. Lusse who performed the visualization tests, Mr. S. Reginato who performed the surface pressure measurements and Mr. C. Beets who performed the grid generation and preliminary computations. The technical staff of the High Speed Laboratory is acknowledged for its technical assistance throughout the experimental part of this project.

CONTENTS

LIST OF SYMBOLS	iv
1 INTRODUCTION	1
2 EXPERIMENTS	2
2.1 Experimental equipment and conventional techniques	2
2.2 Digital Holographic Interferometry	3
3 NUMERICAL FLOW SIMULATIONS	8
3.1 Discretization of the Euler equations	8
3.2 Solution procedure	10
3.3 Computational grid	11
3.4 Numerical simulation of Interferometry	12
4 RESULTS	13
4.1 Visualization studies	13
4.2 Interferometry	18
4.3 Computations	23
4.4 Surface pressure distributions	26
5 CONCLUSIONS	31
REFERENCES	32



LIST OF SYMBOLS

General

bold vectors of variables are indicated in **bold** lowercase
BOLD matrices are indicated in **BOLD** capitals

Arabic

C_L lift coefficient
 C_D drag coefficient
 c speed of sound
 c_p, c_v specific heats at constant pressure and constant volume respectively
 e internal energy
 e_t total energy per unit of mass
 f, g, h flux vectors in x, y, z -direction respectively
 f_{NFF} numerical flux function
 \mathcal{F} spatial discretization of governing equations
 \mathcal{H} Jacobian of discretized system
 h_t total enthalpy
 \mathbf{I} identity matrix
 i, j, k indices in computational space
 K Gladstone-Dale constant
 L width of test-section
 M Mach number
 M_{np} Mach number based on the velocity component in the direction of the local pressure gradient
 N_i, N_j, N_k number of volumes in i, j, k direction respectively
 N_f number of faces of control volume
 \mathbf{n} unit normal vector
 p static pressure
 p_t total pressure
 \mathbf{q} velocity vector
 R gas constant
 r_{ijk}^i limiter function applied to i -direction
 \mathbf{r}_m source term
 S boundary of control volume
 ΔS surface of cell face
 s coordinate along light ray
 \mathbf{T} rotation matrix
 t time
 u, v, w velocity components in x, y, z directions respectively
 V control volume
 ΔV cell volume

x, y, z Cartesian coordinate system
 $\tilde{x}, \tilde{y}, \tilde{z}$ rotated Cartesian coordinate system

Greek

α angle of attack
 γ ratio of specific heats ($c_p/c_v = 1.4$)
 Δ difference operator
 Δ_i, ∇_i forward and backward differences in i -direction
 δ flow deflection angle
 κ constant in higher order interpolation function
 μ Mach angle
 λ wavelength of light source
 ξ parametric coordinate
 ρ density
 ρ_{int} integrated density along light path
 ϕ phase angle
 Ω_{ijk} control volume
 $\partial\Omega$ cell face of control volume

Subscripts

ARS Approximate Riemann Solver
 av averaged quantity
 $dist, undist$ flow field with and without model
 i, j, k grid point indices
 m cell face index
 max maximal
 NFF Numerical Flux Function
 x, y, z components in x, y, z direction
 ∞ free-stream condition

Chapter 1

INTRODUCTION

The present investigation of high-supersonic and hypersonic flows around (blunt) bodies at large angle of attack has been initiated by the development of re-entry spacecraft (Space Shuttle, Hermes) and advanced launchers. In general the flow at these conditions is characterized by several phenomena, such as the presence of a bow shock, embedded shocks, regions of separated and vortical flow, shock-boundary layer and shock-shock interactions and high heating rates near discontinuities at the model surface, such as cockpit-body and wing-body junctions. The prediction of the complex three-dimensional flow field provides a challenging task for numerical methods. In order to validate such computer codes, experimental data of good quality are a prerequisite. For validation of the codes it is satisfactory to study simple configurations, with which interesting flow phenomena can be generated.

Realistic hypersonic flow conditions during re-entry are difficult to simulate in a wind tunnel and require special facilities. Many flow phenomena, such as separation and vortex formation, shock-boundary layer interactions and shock-shock interactions, already appear at high supersonic Mach numbers (3–4). These flow conditions can be realized in standard facilities, for which a variety of measuring techniques is available. In view of these considerations an experimental program on a simple test configuration has been started at the High Speed Aerodynamics Laboratory of the Faculty of Aerospace Engineering. Several wind tunnel tests have been performed on a hemispherical-nose-cylinder with a 30° conical afterbody. Although a simple geometry was selected, several interesting flow phenomena were observed. The leeward flow field at medium to high angle of attack is dominated by large separated regions, vortical flow and embedded shocks. The windward flow field is less complicated, but at large angles of attack an interesting shock-shock interaction exists, which influences the surface flow. The model has been investigated in the high-supersonic flow regime (Mach number 3 up to 4) and angles of attack up to 20°. Under these flow conditions the assumption of a perfect gas is still valid. The purpose of this investigation was to provide aerodynamic data of good quality and high resolution in order to validate computer codes.

Besides the experimental program, a number of numerical simulations with a three-dimensional Euler code have been performed. Within this investigation, emphasis was put on the simulation of inviscid flow phenomena, like the capturing of the bow shock and the flare shock and their interaction at high angles of attack.

The work described in this report has been sponsored by the European Space Research and Technology Centre (ESTEC, Noordwijk, the Netherlands) under Purchase Order number 141125 (date: 28-03-1994). The study was monitored by J. Muylaert, Aerothermodynamics section (YPA) of ESTEC.

Chapter 2

EXPERIMENTS

2.1 Experimental equipment and conventional techniques

The major part of the experiments are performed in the TST-27 wind tunnel of the High Speed Aerodynamics Laboratory. This is a blow-down wind tunnel with a test-section of $27 \times 28 \text{ cm}^2$ (height \times width), which can be operated in the Mach number range $M_\infty = 0.5 - 4$. Interferometric experiments are performed in the ST-15 supersonic blow-down wind tunnel, which has a test-section of $15 \times 15 \text{ cm}^2$. This wind tunnel is equipped with a fixed nozzle, generating a Mach number of 2.95 in the test-section.

The model is axi-symmetric, consisting of a cylinder with a hemispherical head, a conical flare with an angle of 30° and a cylindrical tail. The coordinate system used and the dimensions of the model are given in Fig. 2.1; the dimensions of the model used in the smaller ST-15 wind tunnel are given between brackets. For the tests in the TST-27 wind tunnel two models were made. A solid black-

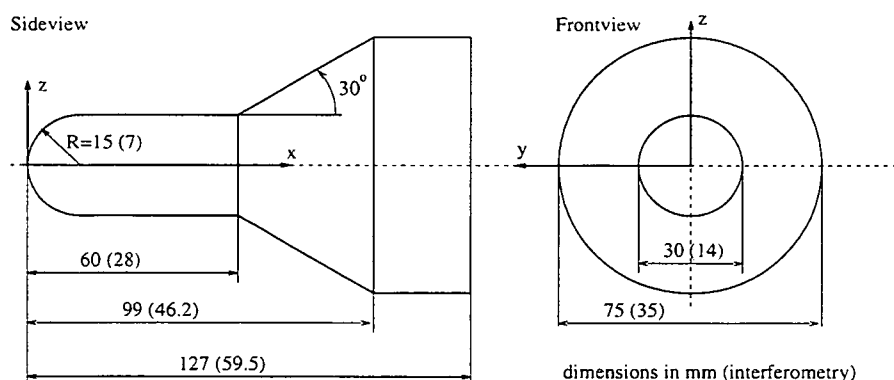


Figure 2.1: Geometry of test configuration

Painted model was used for several experiments, including: qualitative flow visualization as obtained from shadowgraph- and Schlieren techniques, surface oil-flow visualizations and flow field explorations with a five-hole probe (Lusse 1992). Another model was used for measuring the surface pressure distribution (Reginato 1993). This model was equipped with 75 pressure orifices, located at three generators with a 10° spacing (Fig. 2.2). At the rear of the model screw holes allow roll angles with a 360° range and a 5° stepsize, which enables the determination of a pressure distribution over the entire model with a high resolution. The location of pressure orifices is concentrated in regions where a complex (separated) flow was expected, i.e. the region where the hemispherical head changes into the cylindrical part and the region near the conical wedge.

The tests are performed at Mach numbers M_∞ of 3, 3.5 and 4, and angles of attack α from 0° to 20° . The Reynolds number based on a model-length of 127 mm ranges from 6×10^6 to 7.6×10^6 . Part of the results (surface pressures and shadowgraph pictures) is available on demand for validation purposes.

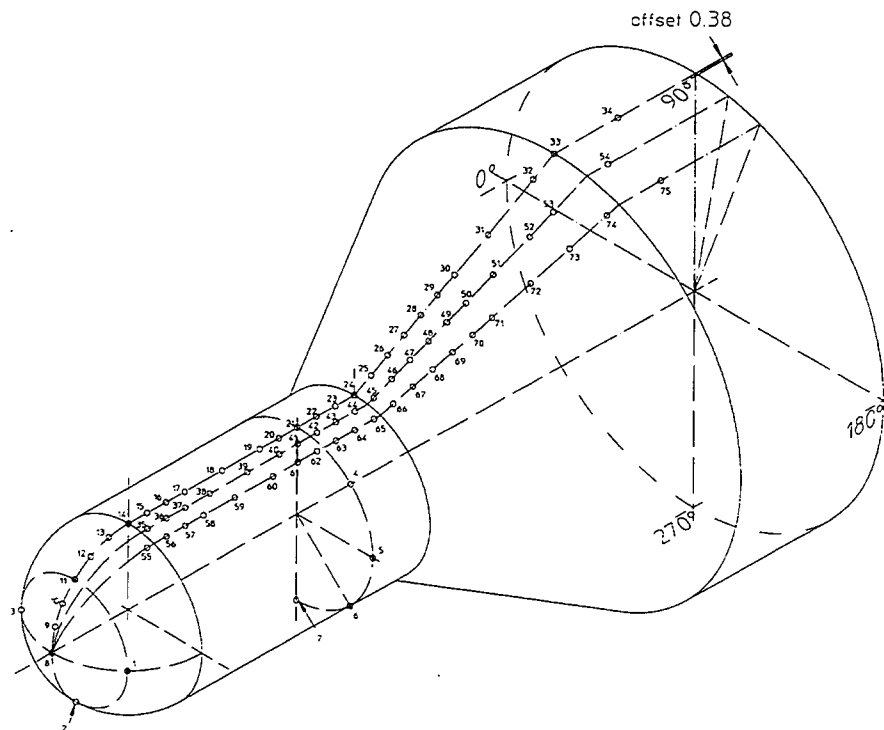


Figure 2.2: Location of pressure orifices on test configuration

2.2 Digital Holographic Interferometry

Digital Holographic Interferometry (DHI) is applied to obtain quantitative information about the density distribution in the flow field. In the dual-reference-beam, plane-wave DHI set-up used here, holographic interferometry for recording of a flow field in an interferogram is combined with phase-stepping of this interferogram and digital image-processing to compute the phase map from these digitised interferograms (Lanen et al. 1992; Lanen 1992). This phase map represents the deformation of the wavefront of the light beam which has traversed the flow field and from it the mean density in the flow field can be calculated. As the results only contain the density integrated along the light paths, quantitative interpretation for 3-D flows is not as direct as in the case of 2-D flows. Main advantage of this optical technique is that a large part of the flow field can be measured at one instant with a high resolution of data and without disturbance of the flow.

The flow field was recorded with the plane-wave holographic interferometer set-up shown in Fig. 2.3. A ruby pulse laser was used to expose the holographic plate, thereby freezing the flow-field image. The pulse length used here is 0.5 msec, resulting in a limited sensitivity to unsteady flow phenomena. In the post-processing phase the plate is illuminated with a (continuous) CW HeNe laser and four phase-stepped interferograms are generated, which are digitally stored and processed. From these four interferograms a 2-D phase image (512×512 pixels, representing a region of $75 \times 75 \text{ mm}^2$ in the flow) is obtained, which contains information about the flow-field density averaged over the light path (tunnel width). The use of two reference paths makes it possible to store two different flow situations on the same holographic plate in such a way that they can be reconstructed separately.

The interferometer set-up is placed over the test section of the wind tunnel. Optical access is provided

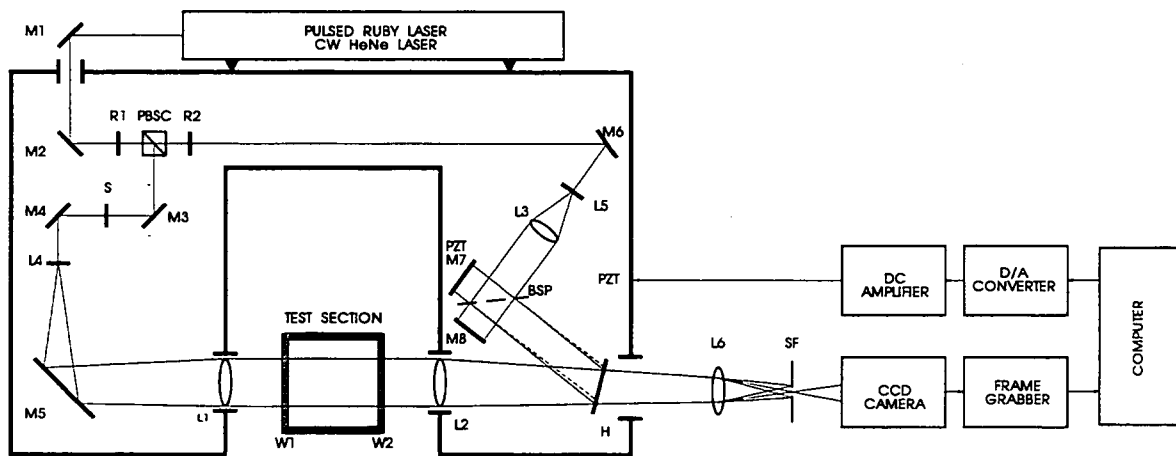


Figure 2.3: Two-reference-beam, plane-wave holographic interferometer. *BSP*: 50/50 beamsplitter plate; *H*: holographic plate; L_1, \dots, L_3, L_6 : positive lens, L_4, L_5 : negative lens; M_1, \dots, M_4 : 45°-incidence HEL-mirror; M_5, M_7, M_8 : mirror; M_6 : 0°-incidence HEL-mirror; *PBSC*: polarising beamsplitting cube; *PZT*: piezo-electric transducer; R_1, \dots, R_3 : $\frac{1}{2}\lambda$ -retardation plate; *S*: mechanical shutter; W_1, W_2 : test-section window; *SF*: spatial filter

by (circular) windows in the tunnel side walls. The main flow direction is normal to the plane of drawing. The model is placed in the middle of the test section. In the reconstruction stage the CCD-camera is focussed at the symmetry plane of the flow, as for axi-symmetric flows this has been shown to minimise refraction problems (Montgomery and Reuss 1982). Hence, the inverse Abel transform can be used to compute the radial refractive index distribution from the interferometric data while neglecting refractive distortion.

The wind tunnel is started with the model in the field of view. With mirror M_8 unblocked the ruby laser is fired once to record the "model flow". Subsequently a recording of the "undisturbed flow" is made, after having retracted the model, out of the field of view (Fig. 2.4), firing the laser for the second time with M_8 blocked and M_7 unblocked. During the reconstruction phase, the object beam is blocked, while both reference beams are recreated by unblocking M_7 as well as M_8 . The plane-wave interferogram resulting from those two reconstructions can be subjected to phase-stepping by translating mirror M_7 , thus enabling an accurate automatic digital computation of the phase shift (Lanen et al. 1992). The method measures the deformation of the wavefront of a (laser) light beam caused by spatial density gradients in the flow field.

Quantitative deduction of the wave front distortion from interferograms requires application of the phase stepping technique to generate at least three phase-stepped interferograms and the application of digital image processing routines to compute the wave front deformation from these digitized interferograms. This procedure overcomes certain ambiguity problems, usually occurring when the evaluation is based on the principle of fringe counting.

In the phase map modulo 2π resulting from phase stepping this "flow" hologram, horizontal background fringes can be seen (Fig. 2.5.a). These result from the difference between the wavelength at which the hologram is recorded ($\lambda_{ruby} = 693.4$ nm) and that at which it is reconstructed ($\lambda_{HeNe} = 632.8$ nm). These background fringes can be removed in two ways. The first one makes use of the fact that the fringe-effect caused by a difference in recording and reconstruction wavelength

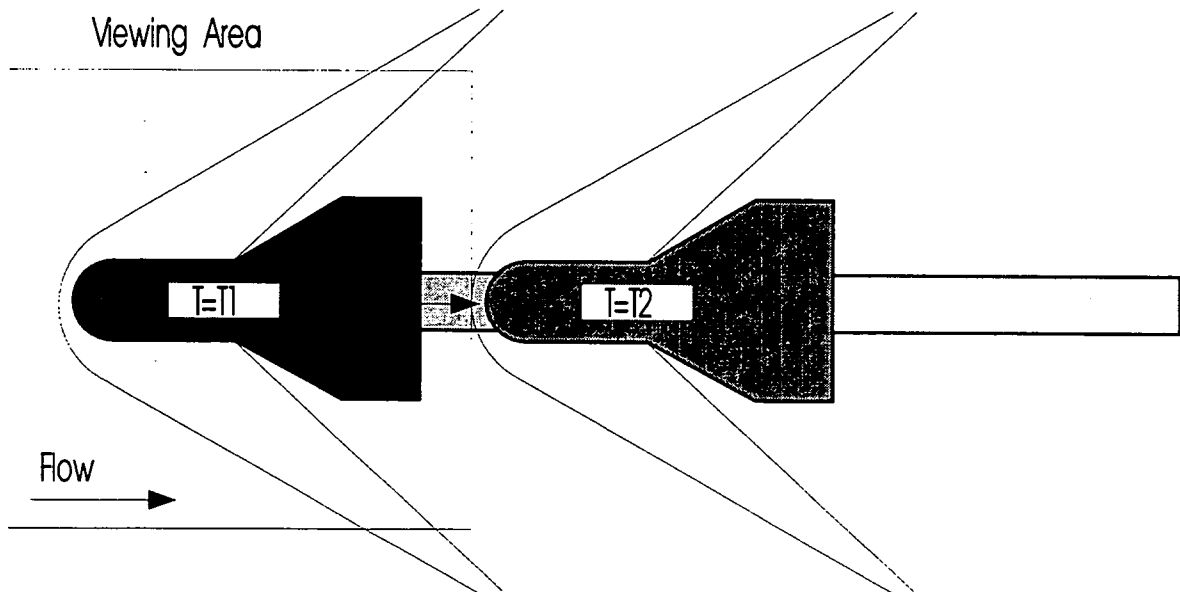
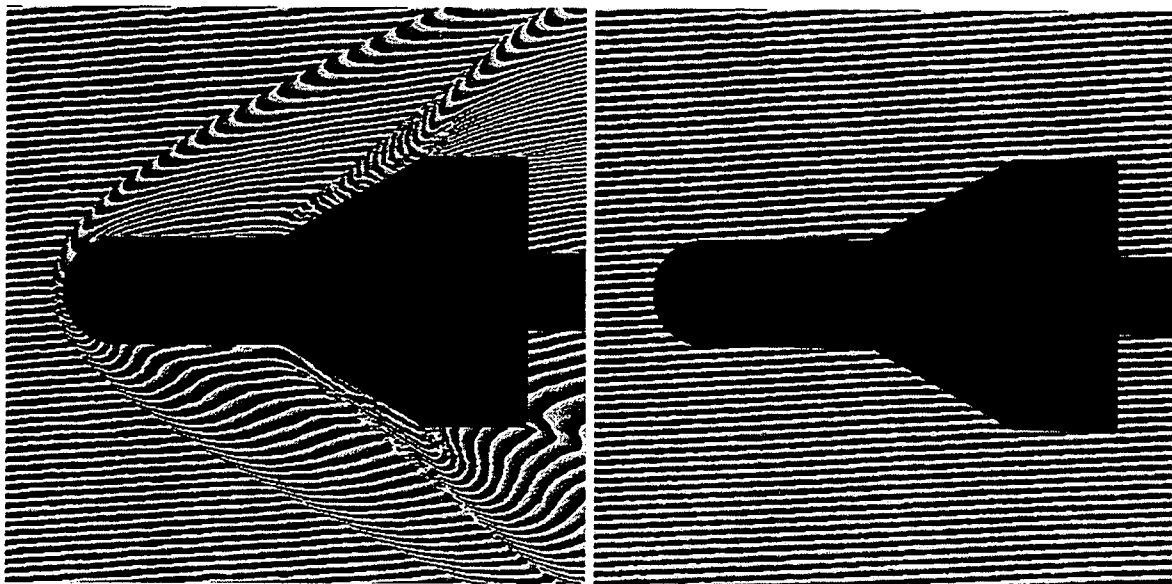


Figure 2.4: Streamwise translation of model between successive exposures of holographic plate



(a) Superimposed linear phase distribution, obtained from "flow" hologram

(b) Reference fringes, obtained from reference hologram

Figure 2.5: Phase maps modulo 2π radians

is similar to that which occurs when the direction of the reconstruction beam differs from that in the recording stage (Françon 1974). Therefore, the background fringes can be eliminated by slightly rotating mirror M_8 , thereby producing an infinite fringe pattern. Phase-stepping and image processing this interference pattern then directly gives the phase modulo 2π . The second solution avoids changing anything to the set-up, by recording an additional hologram of which the reconstructed fringe pattern will only contain the background fringes. This reference hologram is made by two exposures in a no flow situation. By subtracting the phase maps of the reference hologram (Fig. 2.5.b) from the flow hologram, the real phase map modulo 2π is obtained. This second method was used to obtain the results presented in this report.



Figure 2.6: Phase map modulo 2π showing steady deviations from uniform supersonic flow

The phase map (Lanen 1992), which represents the deformation of the wave front of the light beam traversing the flow field (scene beam), may be written as an integral of the refractive index n along the light rays:

$$\Delta\phi(x, z) = \frac{2\pi}{\lambda} \left(\int_{dist} n_{dist} ds - \int_{undist} n_{undist} ds \right) \quad (2.1)$$

Here $\Delta\phi$ denotes the phase difference between the undisturbed scene beam and the disturbed scene beam, λ the wavelength of the pulsed laser, n_{dist} the refractive index in the disturbed flow field (flow with model) and n_{undist} the refractive index in the undisturbed flow field (flow without model). The coordinate s is measured along the light rays and (x, z) represents the projection plane. The refractive index n is linearly coupled to the density ρ via the relation:

$$n = 1 + K\rho \quad (2.2)$$

in which K is the Gladstone-Dale constant, which is a characteristic for the gas through which the light passes. Using this relation, the phase map can be written as a function of the density $\rho(x, y, z)$

in the flow field:

$$\Delta\phi(x, z) = \frac{2\pi K}{\lambda} \left(\int_{-\frac{1}{2}L}^{\frac{1}{2}L} \rho(x, y, z) - \rho_{\infty} ds \right) \quad (2.3)$$

so that the integrated density ρ_{int} along the light path may be determined from the phase angle:

$$\rho_{int} = \frac{1}{L} \int_{-\frac{1}{2}L}^{\frac{1}{2}L} \rho(x, y, z) ds = \rho_{\infty} + \frac{1}{L} \frac{\lambda}{K} \frac{\Delta\phi}{2\pi} \quad (2.4)$$

To assess the quality of the free stream in the wind tunnel, Fig. 2.6 shows the phase map obtained by comparing the undisturbed flow to the no flow situation. It shows an average phase gradient in the flow direction of about one wavelength over 75 mm, which corresponds to a variation in density of 0.02 kg/m^3 (i.e. 3% of the average ρ_{∞} , corresponding to 1% change in M_{∞}). This agrees with earlier pressure probe measurements (Bannink 1963) which showed a decrease in Mach number of 0.4/m in the flow direction. Also, disturbance lines can be seen running at the Mach angle ($\mu_{\infty} = 22^{\circ}$).

Chapter 3

NUMERICAL FLOW SIMULATIONS

3.1 Discretization of the Euler equations

Numerical simulations were performed using a code based on a cell-centred finite-volume discretization of the three-dimensional Euler equations. The Euler equations, expressing conservation of mass, momentum and energy for a compressible perfect gas, will be formulated in conservative form. In a Cartesian coordinate system the Euler equations in a conservative differential form are given by:

$$\frac{\partial \mathbf{q}}{\partial t} + \frac{\partial \mathbf{f}(\mathbf{q})}{\partial x} + \frac{\partial \mathbf{g}(\mathbf{q})}{\partial y} + \frac{\partial \mathbf{h}(\mathbf{q})}{\partial z} = 0 \quad (3.1)$$

where \mathbf{q} is the vector of the conserved variables:

$$\mathbf{q} = (\rho, \rho u, \rho v, \rho w, \rho e_t)^T \quad (3.2)$$

and $\mathbf{f}(\mathbf{q})$, $\mathbf{g}(\mathbf{q})$ and $\mathbf{h}(\mathbf{q})$ are the flux vectors, given by:

$$\begin{aligned} \mathbf{f}(\mathbf{q}) &= (\rho u, \rho u^2 + p, \rho uv, \rho uw, \rho u h_t)^T \\ \mathbf{g}(\mathbf{q}) &= (\rho v, \rho v^2 + p, \rho v u, \rho v w, \rho v h_t)^T \\ \mathbf{h}(\mathbf{q}) &= (\rho w, \rho w^2 + p, \rho w u, \rho w v, \rho w h_t)^T \end{aligned} \quad (3.3)$$

Here ρ is the density; u, v, w are the Cartesian velocity components in the x, y, z directions respectively; p is the static pressure; e_t is the total energy per unit of mass given by $e_t = e + \frac{1}{2}(u^2 + v^2 + w^2)$, in which e is the internal energy per unit of mass; h_t is the total enthalpy given by $h_t = e_t + p/\rho$. For a calorically perfect gas the equation of state may be expressed as:

$$p = (\gamma - 1)\rho e \quad (3.4)$$

in which the ratio of specific heats $\gamma = c_p/c_v$ is considered constant ($\gamma = 1.4$). These equations fully describe the three-dimensional inviscid perfect gas flow.

Solutions of the Euler equations in general may contain discontinuities (shock waves, shear layers). Since the differential form expressed by Eq. (3.1) is not valid at these discontinuities, the equations are written in an integral form, in which discontinuities are captured as "weak" solutions:

$$\iiint_V \frac{\partial \mathbf{q}}{\partial t} dV + \iint_S (\mathbf{f}(\mathbf{q}) \cdot \mathbf{n}_x + \mathbf{g}(\mathbf{q}) \cdot \mathbf{n}_y + \mathbf{h}(\mathbf{q}) \cdot \mathbf{n}_z) dS = 0 \quad (3.5)$$

where $\mathbf{n} = (n_x, n_y, n_z)^T$ with $|\mathbf{n}| = 1$ is the outward unit normal vector on the boundary S of the control volume V . Making use of the invariance of the Euler equations under rotation of the coordinate system, equation Eq. (3.5) can be simplified with:

$$\mathbf{f}(\mathbf{q}) \cdot \mathbf{n}_x + \mathbf{g}(\mathbf{q}) \cdot \mathbf{n}_y + \mathbf{h}(\mathbf{q}) \cdot \mathbf{n}_z = \mathbf{T}^{-1} \mathbf{f}(\mathbf{T} \mathbf{q}) \quad (3.6)$$

where \mathbf{T} is the rotation matrix, which transforms the momentum components of the state vector \mathbf{q} to a new Cartesian \tilde{x} , \tilde{y} , \tilde{z} coordinate system in which the \tilde{x} -axis is aligned with the unit normal on the control volume boundary.

A straightforward and simple discretization of Eq. (3.5) with the substitution of Eq. (3.6) for a subdivision of the control volume V into disjunct cells V_{ijk} (finite volumes) is:

$$\Delta V_{ijk} \frac{\partial \mathbf{q}_{ijk}}{\partial t} + \sum_{m=1}^{N_f} \mathbf{T}_{ijk,m}^{-1} \mathbf{f}(\mathbf{T}_{ijk,m} \mathbf{q}_{ijk,m}) \Delta S_{ijk,m} = 0 \quad (3.7)$$

where ΔV_{ijk} is the volume of cell V_{ijk} , \mathbf{q}_{ijk} is the mean value of \mathbf{q} over V_{ijk} and is collocated at the centre of the finite volume. The second part of the equation is the summation of the total fluxes normal to the surface $\Delta S_{ijk,m}$ of the N_f cell faces of V_{ijk} . This total flux is assumed to be constant over the cell face. For practical reasons (simple implementation) a structured grid with hexahedral cells is used, where $V_{i\pm 1jk}$, $V_{ij\pm 1k}$ and $V_{ijk\pm 1}$ are the neighbouring cells of V_{ijk} . The flux vectors $\mathbf{T}_{ijk,m}^{-1} \mathbf{f}(\mathbf{T}_{ijk,m} \mathbf{q}_{ijk,m})$ in Eq. (3.7) have to be calculated by some numerical flux function. For the calculation of the numerical flux some functions belonging to the family of upwind schemes are used. Three different types of schemes have been implemented in the code: the flux-vector-splitting scheme of van Leer (1982) and flux-difference-splitting schemes of Osher (1982) and Roe (1981). The computations presented in the present report have been obtained with the Osher scheme. In this scheme the numerical flux function for the interface $S_{i+\frac{1}{2}jk}$ may be written in the form:

$$\mathbf{T}_{i+\frac{1}{2}jk}^{-1} \mathbf{f}(\mathbf{T}_{i+\frac{1}{2}jk} \mathbf{q}_{i+\frac{1}{2}jk}) = \tilde{\mathbf{f}}_{i+\frac{1}{2}jk} = \mathbf{T}_{i+\frac{1}{2}jk}^{-1} \mathbf{f}_{NFF}(\mathbf{T}_{i+\frac{1}{2}jk} \mathbf{q}_{i+\frac{1}{2}jk}^L, \mathbf{T}_{i+\frac{1}{2}jk} \mathbf{q}_{i+\frac{1}{2}jk}^R) \quad (3.8)$$

where $\mathbf{q}_{i+\frac{1}{2}jk}^L$ and $\mathbf{q}_{i+\frac{1}{2}jk}^R$ are the states at either side of the cell interface, obtained from an interpolation between some states \mathbf{q}_{ijk} in the centres of the finite volumes. For example, in a spatially first order accurate system, the states are assumed to be constant within each volume, so we get $\mathbf{q}_{i+\frac{1}{2}jk}^L = \mathbf{q}_{ijk}$ and $\mathbf{q}_{i+\frac{1}{2}jk}^R = \mathbf{q}_{i+1jk}$.

First order accuracy, however, is too low for practical applications and discontinuities not aligned with the grid are smeared out disastrously. As has been noted by van Leer (1977) the order of accuracy can be improved by using a more accurate interpolation to calculate the different components q of the state vectors \mathbf{q} at both sides of a cell face. In order to avoid spurious non-monotonicity (wiggles or over- and undershoots), the interpolation has to be limited, which has the properties of second order accuracy in the smooth part of the flow field and steepening of discontinuities without introducing non-monotonicity. For the present calculations the MinMod limiter function is used, which had been chosen for reasons of efficiency. The interpolation formulae for the MinMod limiter are:

$$q_{i+\frac{1}{2}jk}^L = q_{ijk} + \frac{1}{4} \{ (1 + \kappa) \bar{\Delta}_i + (1 - \kappa) \bar{\nabla}_i \}$$

$$q_{i+\frac{1}{2}jk}^R = q_{ijk} - \frac{1}{4} \{ (1 - \kappa) \bar{\Delta}_i + (1 + \kappa) \bar{\nabla}_i \}$$

where

$$\bar{\Delta}_i = \text{MinMod}(\Delta_i, \nabla_i) \quad ; \quad \bar{\nabla}_i = \text{MinMod}(\nabla_i, \Delta_i) \quad (3.9)$$

and the MinMod-function is given by:

$$\text{MinMod}(x, y) = \text{sign}(x) \cdot \max[0, \min(x \cdot \text{sign}(y), y \cdot \text{sign}(x))] \quad (3.10)$$

3.2 Solution procedure

The system of nonlinear discretized equations is solved by means of a multigrid technique. Although not well-established for hyperbolic differential equations, the multigrid technique has been applied successfully to the Euler equations (Anderson et al. 1988; Spekreijse 1987; Hemker and Koren 1995). The advantage of a multigrid solution method is that (at least for the first-order discretized Euler equations) a convergence rate is achieved, which is independent of the mesh size at quite general circumstances.

Consider the first- or second order accurate discretization of the Euler equations given by equation Eq. (3.7) to be written as:

$$\Delta V_m \frac{\partial \mathbf{q}_m}{\partial t} + \mathcal{F}_m(\mathbf{q}_m) = 0 \quad (3.11)$$

where \mathcal{F}_m is the spatial discretization operator at gridlevel m . A nested sequence of finite volume grids V_m ($m = 1, \dots, n$) is developed, with corresponding mesh sizes $h_1 > h_2 > \dots > h_n$. Hence V_1 is the coarsest grid and V_n is the finest grid. The grids have a regular structure for reasons of simple implementation. Each finite volume on a given grid is the union of eight volumes on the next finer grid by skipping every other point in each direction on the finer grid.

The solution of the discretized equations is achieved by a Nonlinear MultiGrid method (NMG), also known as Full Approximation Scheme (FAS). In order to start with a good initialization, the NMG is preceded by a nested iteration. The nested iteration starts at the coarsest grid with an initial \mathbf{q}_m ; $m = 1$. The approximate solution \mathbf{q}_m is improved by a single NMG-cycle. The approximate solution \mathbf{q}_{m+1} on the next finer grid is obtained by a prolongation of the approximate solution \mathbf{q}_m ; this is achieved by a trilinear interpolation.

Within the multigrid method, the solution at the different grid levels is smoothed by a relaxation method. Relaxation methods have very good stability and (error) smoothing properties, and although the computational costs per iteration are higher, the overall performance may defeat an explicit time-integration method.

The smoothing procedure used here is based on an implicit time integration method. For the system of equations Eq. (3.11) a backward time-integration method can be written as:

$$\Delta V_j \frac{\Delta \mathbf{q}_j^{n+1}}{\Delta t} = -\mathcal{F}(\mathbf{q}_j^{n+1}) \quad (3.12)$$

where $\mathcal{F}(\mathbf{q}_j^{n+1})$ denotes the spatial discretization evaluated at time level $n+1$, and $\Delta \mathbf{q}_j^{n+1} = \mathbf{q}_j^{n+1} - \mathbf{q}_j^n$. Because Eq. (3.12) is a system of non-linear equations, this cannot be solved directly. Therefore a Newton linearization is used, which can be written as:

$$\mathcal{F}(\mathbf{q}_j^{n+1}) = \mathcal{F}(\mathbf{q}_j^n) + \left[\frac{\partial \mathcal{F}}{\partial \mathbf{q}} \right]_j^n \Delta \mathbf{q}_j^{n+1} \quad (3.13)$$

Substitution of Eq. (3.13) into Eq. (3.12) with $\mathcal{H} = \left[\frac{\partial \mathcal{F}}{\partial \mathbf{q}} \right]_j^n$ gives:

$$\left[\frac{\Delta V_j}{\Delta t} \mathbf{I} - \mathcal{H} \right]_j^n \Delta \mathbf{q}_j^{n+1} = -\mathcal{F}(\mathbf{q}_j^n) \quad (3.14)$$

For the limit $\Delta t \rightarrow \infty$ Newton's root finding method is obtained, which should theoretically lead to quadratic convergence if the Jacobian matrix \mathcal{H} is evaluated correctly. The system Eq. (3.14) represents a large banded block matrix, whose bandwidth is dependent on the order of accuracy of the spatial discretization and on the dimensions of the grid. Especially for the three-dimensional second-order discretized equations the bandwidth is very large. The construction of this matrix and solving the system requires an enormous amount of memory and CPU-time, which goes far beyond the capacities of most computers. Rather than solving Eq. (3.14) directly, a number of strategies have been developed in order to reduce the computational work, but maintaining a high convergence rate as far as possible. When second order accurate steady solutions are required, it is common practice to replace the true Jacobian matrix \mathcal{H} in the left hand side of Eq. (3.14) by a much simpler matrix \mathcal{H}^1 based on the first-order accurate equations. For steady flows this has no effect on the accuracy of the right hand side discretization. The matrix for a three-dimensional first-order system is a septadiagonal block matrix, where the blocks itself are 5×5 -matrices. However, certainly for three-dimensional problems this system is still too large to solve directly, so most implicit methods use iterative methods. In this report a Collective point Gauss-Seidel relaxation method has been used, with an ordering of the relaxation sweeps along diagonal planes in order to achieve some level of vectorization.

3.3 Computational grid

A view of the grid is given in Fig. 3.1, where the grid on the surface of the model, in the symmetry plane and in the outflow plane is shown. The majority of the computations is performed on a grid

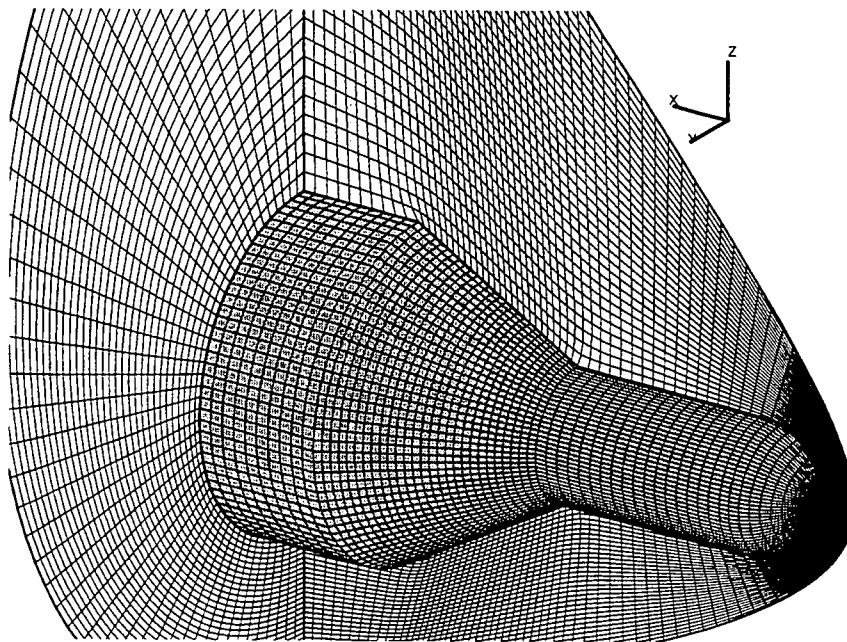


Figure 3.1: Three-dimensional view on grid; $64 \times 48 \times 32$ cells

with 64 cells in the direction of the rotation axis, 48 cells in the circumferential direction and 32 cells in the direction normal to the surface. The grid is constructed with an elliptic grid generator based on the Poisson equation, which uses an initial solution obtained by a 3D transfinite interpolation.

3.4 Numerical simulation of Interferometry

Since the experimental DHI technique delivers an integrated density, which is not a direct output of the numerical simulation, it is necessary to post-process the numerical results, in order to be able to compare experimental and numerical results. The computation of the numerical phase map is based on Eq. (2.3), which will be evaluated for a number of lines equal to the number of pixels in the experimental phase map. This procedure makes a direct comparison between experimental and numerical results possible. Comparison of experimental and calculated phase maps serves a two-fold purpose. In addition to the validation of the calculations it can assist in the interpretation of the experimental data.

The parameters needed for computing the phase map from the 3-D density field around the body, $\rho(x, y, z)$, are the Gladstone-Dale constant for air, K ($0.2251 \times 10^{-3} \text{ m}^3/\text{kg}$), the wavelength of the laser, λ ($693.4 \times 10^{-9} \text{ m}$) and the free stream density, ρ_∞ (0.70 kg/m^3).

The evaluation of the integral Eq. (2.3) should be performed along the actual light paths. The actual light path is bent due to refractive-index gradients. Formally this path through the flow field should be traced, and the refractive index gradient (or density gradient) should be integrated along this path, but this is a computationally very expensive procedure. The computational complexity can be reduced considerably by approximating the light path by a straight line perpendicular to the image plane (along the y -axis).

In order to evaluate integrals along straight lines through a discrete field, an algorithm has been written which calculates the values of the appropriate integrand at certain points, after which the integration is performed according the trapezoidal rule. This process is schematically shown in Fig. 3.2. The Euler code described above uses a grid with hexahedral cells. For the interpolation procedure,

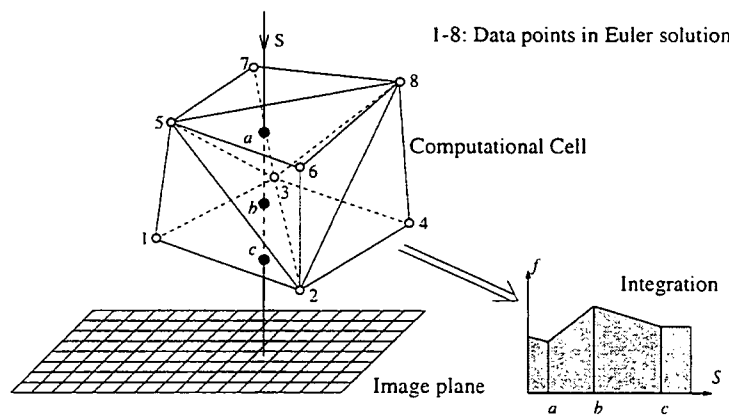


Figure 3.2: Schematic View of Integration Process

each computational cell is subdivided into five tetrahedrals. The integration procedure follows a path along subsequent triangular cell faces of the tetrahedrals. The intersection of the light path with the triangular cell face is determined (points a , b and c in Fig. 3.2) and the desired quantity is calculated via a linear interpolation between the nodes of the triangular cell face. This cell-face to cell-face interpolation algorithm makes the search algorithm much faster than an interpolation based on a fixed interval spacing along the light paths. Furthermore the accuracy of the integration along the light ray is automatically adjusted to the accuracy of the discrete Euler solution.

Chapter 4

RESULTS

Before discussing the interferometry- and computational results, some results of the qualitative flow visualization tests will be presented, in order to highlight the global flow structure and some interesting flow phenomena.

4.1 Visualization studies

In Fig. 4.1 the most significant shadowgraphs taken at a very short exposure (20 nanoseconds) are given for flows at Mach numbers $M_\infty = 3$ and 4 and angles of attack of 10° , 15° and 20° . These pictures clearly show the bow shock and the flare shock, and their interaction at the windward side for $\alpha = 15^\circ$ and $\alpha = 20^\circ$. The flow features drawing attention are the unsteady character of the leeward flow, where the flow separation from the cylinder and attachment at the conical flare is coupled with a number of weak shocks. Apparently we have to do with a transitional flow. This unsteadiness may also be observed at the windward side for a certain combination of Mach number and angle of attack as shown by the flare shock at the vertex of the flare. The unsteadiness is present at all angles of attack at $M_\infty = 3$ and only at $\alpha = 20^\circ$ at $M_\infty = 4$. The flow separation at the leeward side may be observed by means of the weak separation shock and the edge of the separated flow. The weak separation shock is clearly present in all cases, except at $M_\infty = 4$ and $\alpha = 20^\circ$ and extends from the separation point to the flare shock. The front part of the separation zone shows itself as a very thin layer which suddenly dissolves more or less halfway the cylinder, indicating probably the transition from laminar to turbulent flow. The shadowgraphs show a tendency that the transition region moves upstream with increasing angle of attack.

The shock-shock interaction at the windward side moves upstream and closer to the surface with increasing angle of attack and with increasing free-stream Mach number. At an angle of attack of 20° and at $M_\infty = 4$ and $\alpha = 15^\circ$ the shock-shock interaction has an effect on the flare surface via an adjustment wave, originating from the interaction point. This adjustment wave is clearly visible in the shadowgraphs. Interactions between two shocks can be classified into several types, depending on the Mach number of the oncoming flow and the angles of the two impinging shocks (Edney 1968). A type VI interaction (see Fig. 4.2.b) takes place when both shocks are sufficiently weak and of the same family. This type of interaction produces a combined shock, a slip line and an adjustment wave emanating from the shock intersection point. Depending on the geometrical configuration and free stream Mach number the adjustment wave appears either as a compression shock or as an expansion fan. A type V interaction (see Fig. 4.2.a) can occur when the flare shock is sufficiently strong. Here, the interaction region is more complex and from it four different elements emanate: a curved combined shock, an extra shock, a shear layer and a jet (a small layer containing compression and expansion waves). The jet and the shear layer almost coincide.

A detail of the shock-shock interaction area at $M_\infty = 4$ and $\alpha = 20^\circ$ is shown in Fig. 4.3. This interaction may be investigated by the use of Edney's pressure flow deflection diagrams (Edney 1968), which gives the pressure rise and flow deflection through one or more oblique shock waves. The

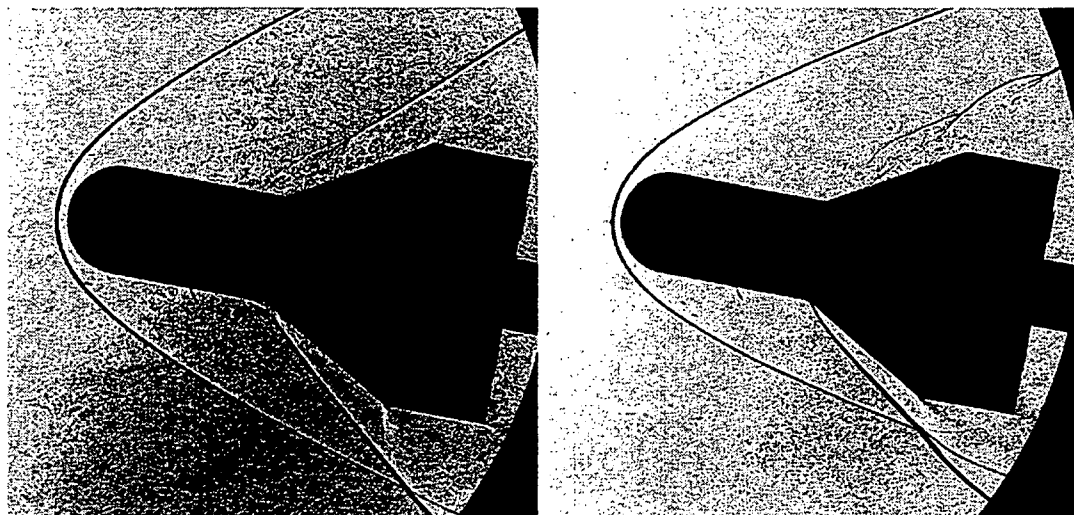
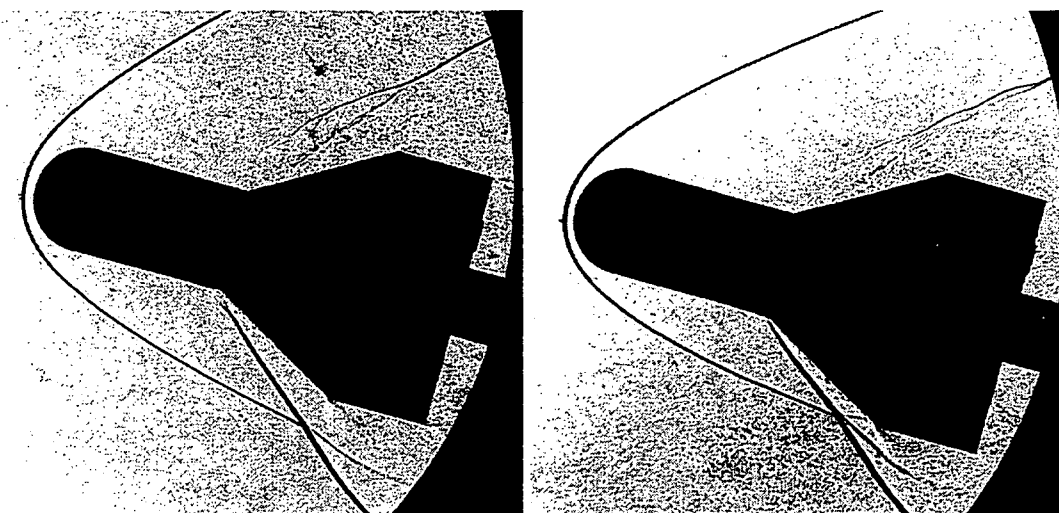
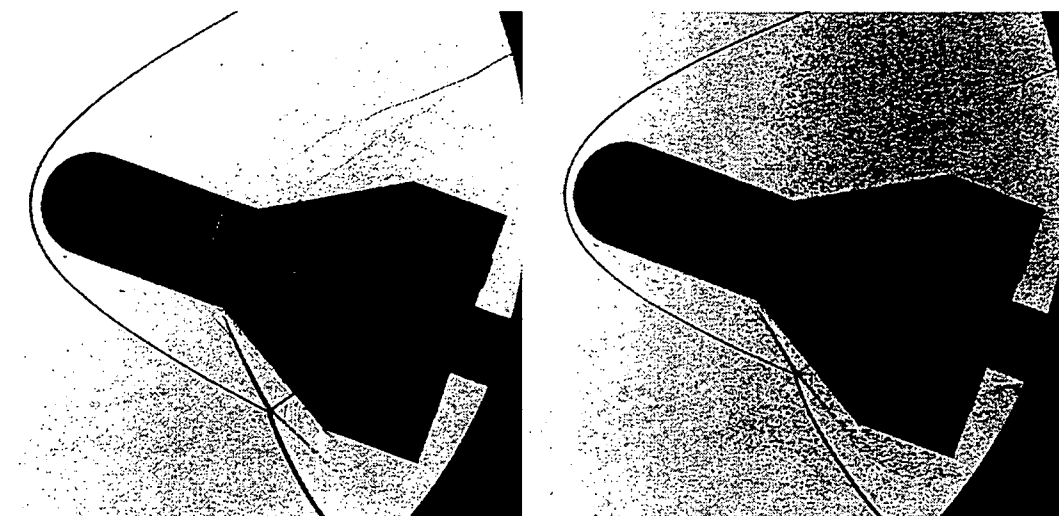
(a) $M_\infty = 3, \alpha = 10^\circ$ (b) $M_\infty = 4, \alpha = 10^\circ$ (c) $M_\infty = 3, \alpha = 15^\circ$ (d) $M_\infty = 4, \alpha = 15^\circ$ (e) $M_\infty = 3, \alpha = 20^\circ$ (f) $M_\infty = 4, \alpha = 20^\circ$

Figure 4.1: Spark-shadowgraphs

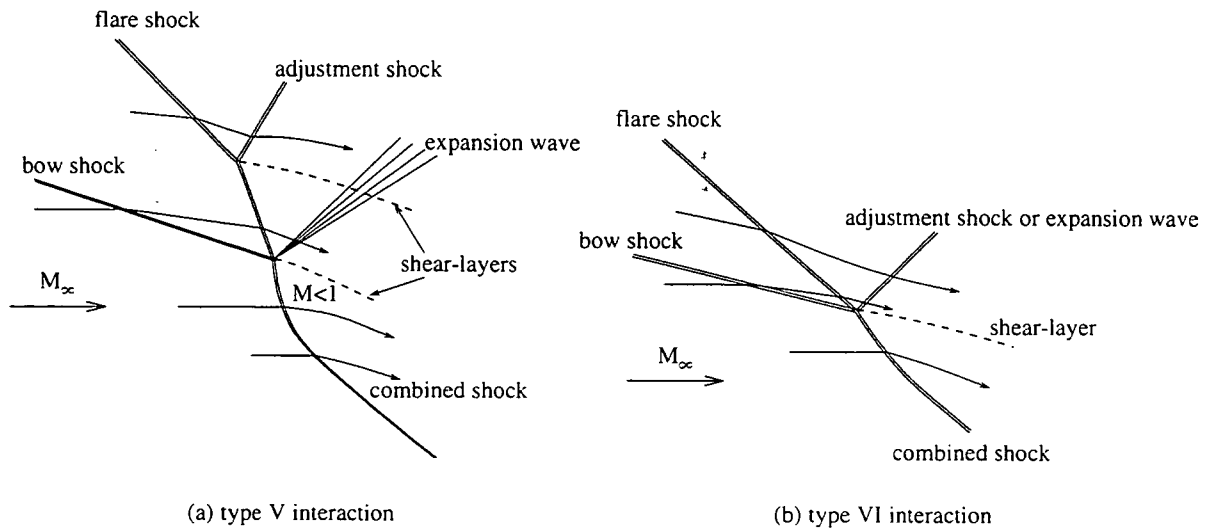


Figure 4.2: Sketches of different shock-shock interactions (Edney 1968)

pressure-flow-deflection diagram for the case $M_\infty = 4$ and $\alpha = 20^\circ$ is shown in Fig. 4.4, which is based on the measurement of the shock angles of the bow shock, the flare shock and the combined shock near the interaction point. The static pressure p behind an oblique shock is plotted as a function of the flow deflection δ through a shock, giving a heart-shaped curve. The shock-polar for the free-stream Mach number, which is 3.96 in the present case, is shown, and other shock-polars are given relative to the free-stream shock-polar. From the measured bow shock angle near the interaction, point 1 on the free-stream shock-polar can be found. At this point the deflection angle and static pressure are defined behind the bow shock. Point 1 serves as a starting point for another curve, which is a function of the Mach number and deflection angle behind the bow shock. In a similar way point 2, which defines the flow deflection and static pressure behind the flare shock, can be found. Using the angle of the combined shock, point 4 can be found on the free-stream shock-polar. The flow behind this part of the shock appears to be subsonic. If it is assumed that no other waves depart from the interaction point S , the pressures in the regions 3 and 4 should be equal. Since the pressure in region 2 is lower than the pressure in region 4, a shock wave is needed between regions 2 and 3 in order to establish the required pressure. This type of interaction was classified by Edney (Edney 1968) as a type VI interaction. It must be emphasized that the flow-deflection diagram is only valid in the interaction point, because of the three-dimensionality of the flow.

However, studying the detailed shadowgraph of the interaction Fig. 4.3, there may be some evidence that the bow shock, the flare shock and the adjustment wave do not intersect in a single point, but in two different points. The structure belonging to this type of interaction is the much more complex type V interaction, which can not be analyzed using only the shadowgraph information, since starting conditions at the flare shock are unknown. As can be seen in the sketch of this type of interaction (Fig. 4.2.a) two adjustment waves start from the interaction region. These two waves, a shock wave and an expansion wave are also visible in the shadowgraph picture. Furthermore, the appearance of a weak adjustment shock and an expansion wave is supported by other experiments (oil-flow and surface pressures), which will be presented further on.

The oil-flow visualization tests reveal a complex separation pattern at angles of attack above 5° . The

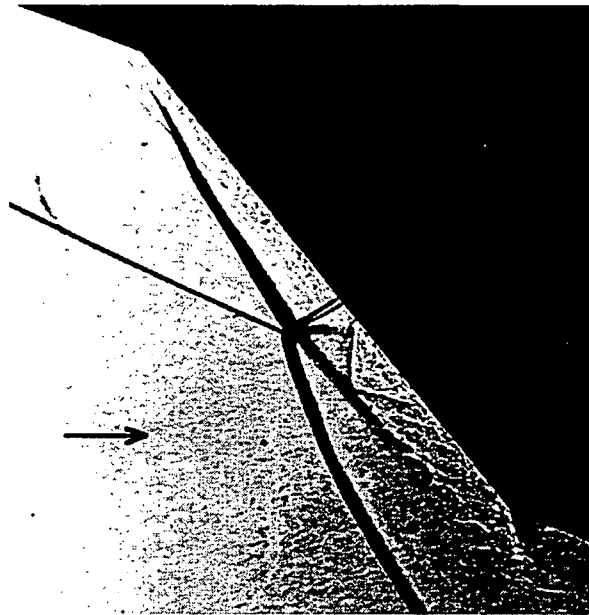


Figure 4.3: Spark-shadowgraph of the shock-shock interaction, $M_\infty = 4$, $\alpha = 20^\circ$

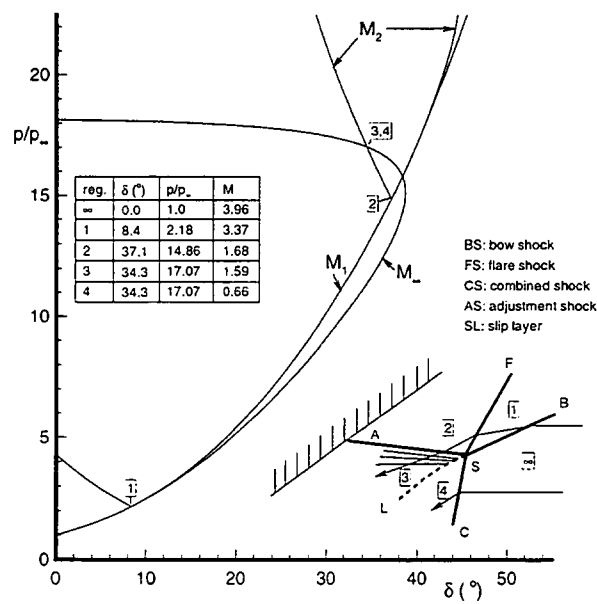


Figure 4.4: Pressure-flow deflection diagram of shock-shock interaction at windward side;
 $M_\infty = 4$, $\alpha = 20^\circ$

oil-flow pictures at the leeward- and windward side for $M_\infty = 4$ and $\alpha = 20^\circ$ are given in Fig. 4.5 and Fig. 4.6 respectively. Based on the leeward oil-flow picture a proposition of the surface topology

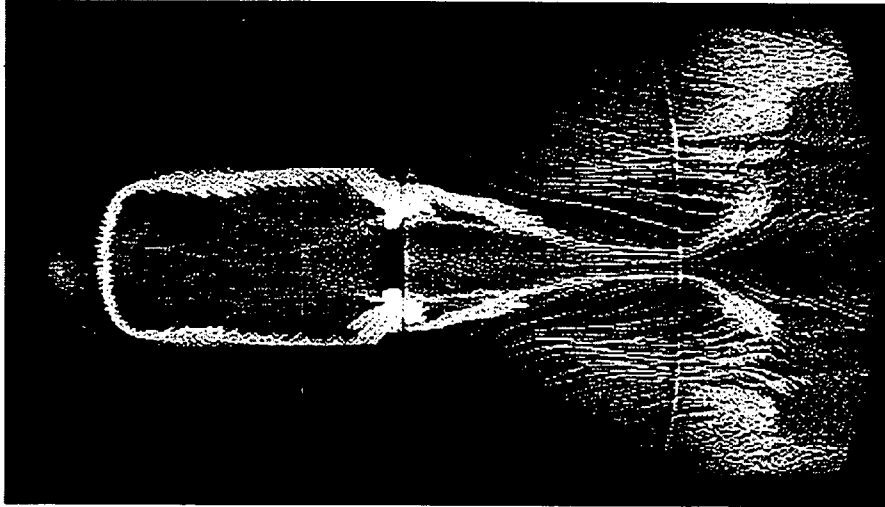


Figure 4.5: Oil-flow visualization leeward side, $M_\infty = 4.04$, $\alpha = 20^\circ$

is arranged (Bakker and Bannink 1992) in Fig. 4.7. A primary separation starts from a saddle point (S_s) at the leeward side of the cylindrical part directly behind the hemisphere. This type of separa-

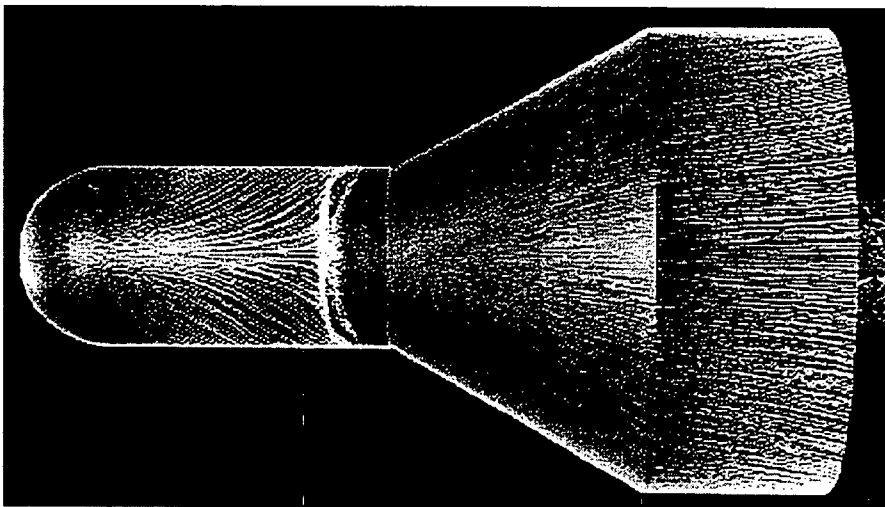


Figure 4.6: Oil-flow visualization windward side, $M_\infty = 4.04$, $\alpha = 20^\circ$

tion is characteristic for hemispherical cylinders at large angle of attack. Pairs of saddles (S_s) and foci (N_s) signal the formation of vortices emerging from the body surface. At the windward side a separation line is visible (Fig. 4.6) at the aft part of the cylinder. This separation is probably caused by the existence of the flare shock. The separation lines at the windward and leeward side pass into each other. On the flare cone a reattachment occurs on both sides. Downstream of this reattachment, separation lines can be observed at the leeward side, which diverge at the cylindrical aft part.

The effect of the adjustment shock originating from the shock-shock interaction is visible as a dark line

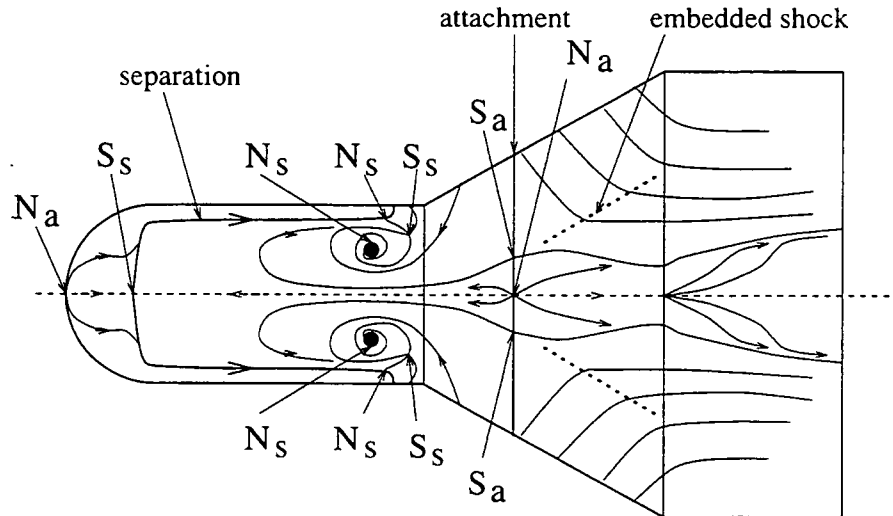


Figure 4.7: Proposition for leeward side surface topology, $M_\infty = 4$, $\alpha = 20^\circ$

in the oil-flow pattern on the windward conical flare surface. This position coincides with intersection of the adjustment shock and the surface as was observed in the shadowgraph Fig. 4.3.

4.2 Interferometry

Figures 4.8 (a) and (b) show the results of the interferometric experiments and the postprocessed numerical calculations, respectively, for the axi-symmetric flow case (0° angle of attack). In the experimental phase map modulo 2π the model has been depicted in black. It further contains some areas (near the shock waves) where the fringes are so closely packed that no separate fringes can be discerned. These areas do not satisfy the sampling criterion (i.e. the minimum sampling frequency must be higher than 2 pixels/fringe) required in order to remove the 2π discontinuities correctly from the phase map modulo 2π (phase unwrapping), and therefore have to be circumvented in this process. In pixels with a low value of the modulation intensity (this also follows from the phase-stepping procedure (Lanen et al. 1990)), the phase value is unreliable. Low modulation intensity areas can be found in regions where light rays are blocked by the model and in regions of insufficient sampling (high gradients, e.g. near shocks). Therefore the position of the model and the unreliable pixels can be determined by thresholding the modulation intensity. By doing so a mask is obtained containing the pixels that have to be circumvented in the phase unwrapping process. In the following interferometric results the unreliable pixels will be depicted in black, not to be confused with the fringe pixels with value $2n\pi$, with n a natural number.

Direct comparison of measured and computed phase maps is inhibited by two error sources in the experimental data: non-uniformities in the free stream and the presence of unreliable areas. From the mask in Fig. 4.9 a it appears that not all pixels on the bow shock are unreliable. However, phase-unwrapping attempts fail to pass the shock correctly. Therefore in all results presented here the phase map modulo 2π will be shown instead of the continuous phase map. This means that the comparison with numerical results can only reveal whether the behaviour of the flow inside the reliable areas is the same for both techniques.

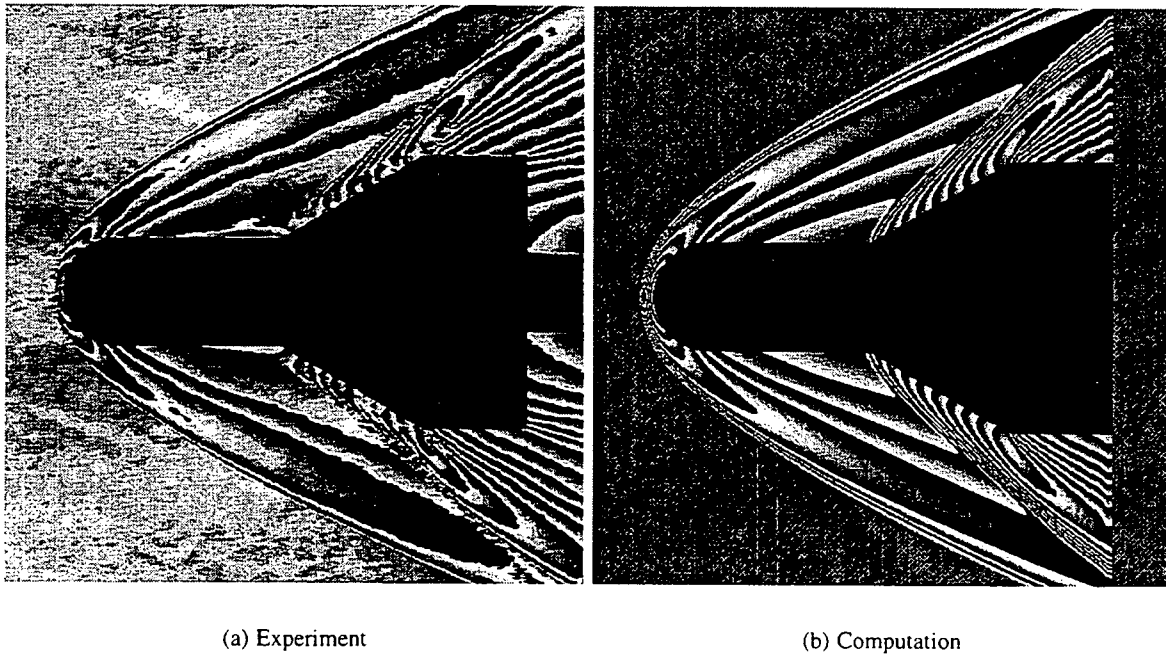


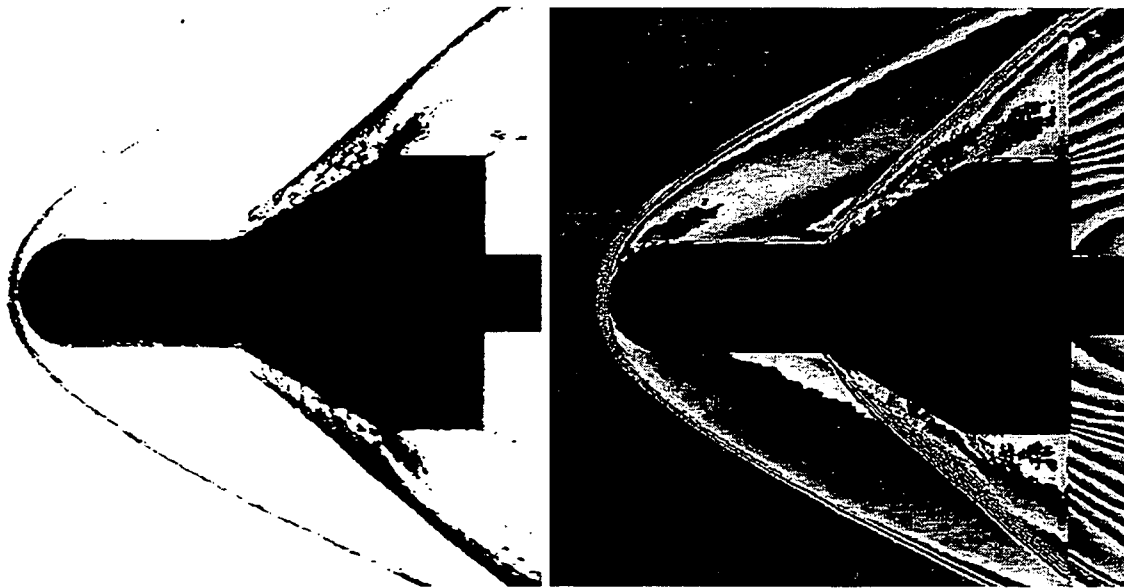
Figure 4.8: Phase maps modulo 2π , $M_\infty = 2.95$, $\alpha = 0^\circ$

An example of a mask is given in Fig. 4.9 a for the zero angle of attack case. From the mask a strengthening of the flare shock can be seen which is caused by the impingement of the expansion fan from the nose region due to the increase of local shock angle and Mach number. Between the nose and the bow shock the phase map modulo 2π seems to give continuous fringes, but these have to be cancelled because of unreliability.

Also the flare shocks and the shock-shock interaction area give no reliable results. An explanation for this can be found in the numerical phase map: the gradient is very high in those areas, which results in a very close spacing of the fringes, so that the limit of 2 pixels per fringe cannot be reached. This could not be helped sufficiently by zooming in on these areas. Therefore, as little or no extra information could be gained from zooming, all results are presented covering the same area: $75 \times 75 \text{mm}^2$. The blurred regions at the cone surface might be due to unsteady flow phenomena, such as a turbulent boundary layer.

Fig. 4.9 b shows a pixelwise comparison by subtracting the measured and the computed phase maps. It can be seen that, apart from the shock areas, the results agree reasonably well. However, the differential phase map shows substantial differences in the vicinity of the shock waves, especially at the bow shock near the stagnation point and at the flare shock. The numerical phase map shows a more gradual phase difference gradient at the shock than the experimental phase map. Also, the differential phase map is seen to be slightly asymmetric. This is caused by the fact that the angle of incidence was not exactly 0° (namely 0.45°) and by the non-uniformity of the free stream.

Differences between the numerical and experimental phase maps can also be expected in regions of the flow field where viscous effects are present. For the axi-symmetric flow case these regions are confined to the boundary layer, which influences the flare shock. The correspondence between the shock locations is good. The results only differ at the foot of the flare shock. Due to the presence of a



(a) Binary mask indicating the location of model and unreliable pixels, $M_\infty = 2.95$, $\alpha = 0^\circ$

(b) Differential phase map modulo 2π derived from subtracting the computational solution from the measured phase map

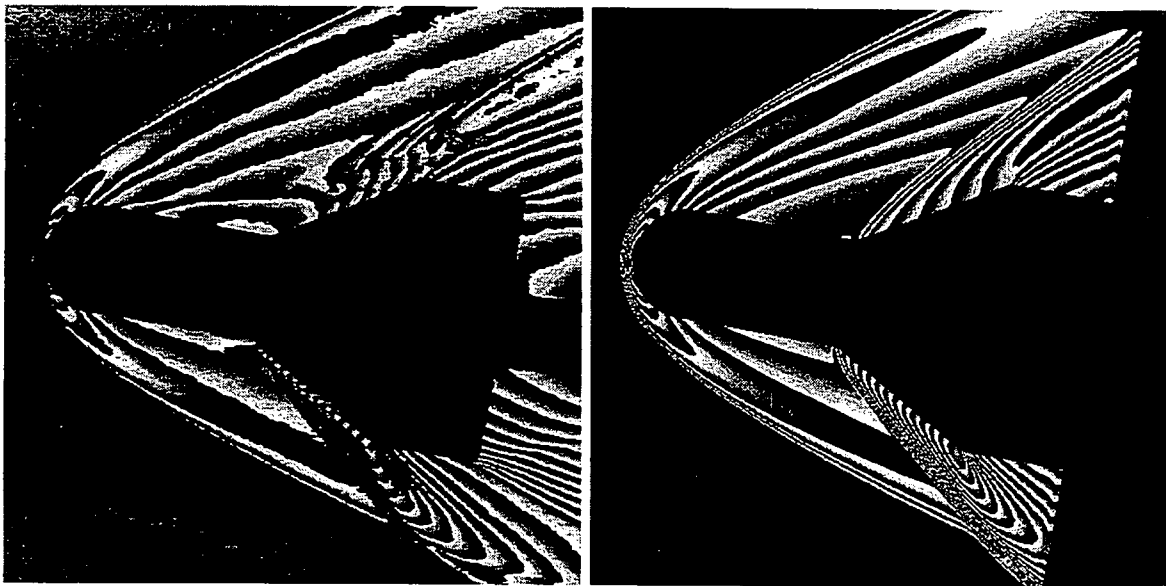
Figure 4.9: Binary mask and differential phase map, $M_\infty = 2.95$, $\alpha = 0^\circ$

boundary layer the flare shock in the experiment is formed at some distance from the model surface.

In general a strong bending of the interference fringes towards the surface is observed (Lanen and Houtman 1992) as a result of the temperature gradient in the boundary layer. The present result also shows this behaviour, especially at the flare surface where the experimental, turbulent boundary layer is thick. The differential phase map (Fig. 4.9 b) clearly shows that the influence of the boundary layer is most pronounced over the flare surface. The small separation of the flow at the strong expansion wave is also visible, which is not present in the numerical computations.

Similar experiments have been performed for several non-zero angle of attack flows. Figures 4.10 and 4.11 show the results of the interferometric experiments and the postprocessed numerical calculations, for the flow at $M_\infty = 2.95$ and $\alpha = 10^\circ$ and $\alpha = 20^\circ$, respectively. It can be seen that on the windward side the unreliable area of the flare shock is expanding with increasing angle of incidence. An unreliable area also occurs at the flare cylinder connection, where an expansion of the flow causes a strong density gradient.

For the 3-D flow field the influence of viscosity is no longer restricted to the vicinity of the model surface. A comparison of the results shows that the viscous areas are captured very well by interferometry, whereas they are obviously not by the numerical code. Flow separation at the leeward side occurs just downstream of the nose and shows up clearly in the interferometric results. Even though the unreliable area at the windward side becomes rather large, some information can be gained from these unreliable parts, because of the sharp boundary between reliable and unreliable pixels near the shock waves. Especially at an angle of attack, when the area behind the intersection comes into view, some signs of the phenomena emanating from the interaction can be seen (also in the numerical re-



(a) Experiment (unreliable pixels depicted in black)

(b) Computation

Figure 4.10: Phase maps modulo 2π , $M_\infty = 2.95$, $\alpha = 10^\circ$ 

(a) Experiment (unreliable pixels depicted in black)

(b) Computation

Figure 4.11: Phase maps modulo 2π , $M_\infty = 2.95$, $\alpha = 20^\circ$

sults).

At the windward side of the model there is a reasonable correspondence of the experimental and numerical shock locations, although the numerical flare shock seems to be positioned further from the body. This may be caused by the fact that in the experimental results the flare shock is not attached to the model, whereas it is for the numerical flow field. In the experimental results the flare shock is formed closer to the model surface than for $\alpha = 0^\circ$ which is probably due to a thinner upstream boundary layer. The numerical results now yield a detached shock, which is the correct non-viscous solution. Both the numerical and the experimental results show that the flare shock strength increases at the shock-shock interaction. Further downstream the flare shock becomes weaker due to the interaction with the expansion wave originating at the cone-cylinder junction. At the leeward side of the model the flare shock is formed at a considerable distance from the model surface due to the large scale flow separation. The non-viscous results of the Euler Code still yield a shock wave which can be traced up to the model surface.

In the interferometric measurements there seems to be some structure at the leeward side of the model aligned with the flare. Here the unreliable, flare shock area does not possess the narrow shock-like structure but has a more wavy character. Especially at an angle of 20° it gives a "vortical" impression. Topological interpretations of earlier oil-flow experiments reveal the presence of two counter rotating vortices originating from the separation region at the leeward side of the model (Bakker et al. 1992), which may explain this pattern. In the interferometric results these structures show up as unreliable pixels because they occur outside the symmetry plane at which the set-up is focussed. As they are not imaged properly a shadowgraph-effect occurs due to light ray deflection. Although no quantitative information can be extracted from these points, some insight into the form and behaviour of these vortical structures may be gained.

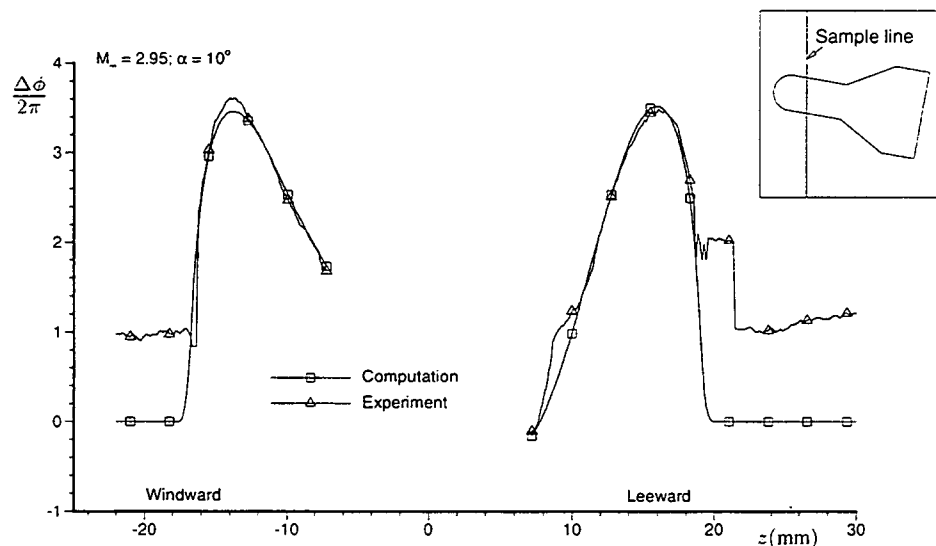


Figure 4.12: Unwrapped phase along vertical line, $M_\infty = 2.95$, $\alpha = 10^\circ$

The unwrapped phase angle ($\Delta\phi/2\pi$) along a vertical line through the cylindrical part (indicated in the small figure inserted) has been plotted in Figs. 4.12 and 4.13 for $\alpha = 10^\circ$ and $\alpha = 20^\circ$, respectively. The phase angle $\Delta\phi$ is related to the integrated density along the light paths according to Eq. (2.4). The experimental phase distribution has been shifted 2π and 4π radians for $\alpha = 10^\circ$ and $\alpha = 20^\circ$,

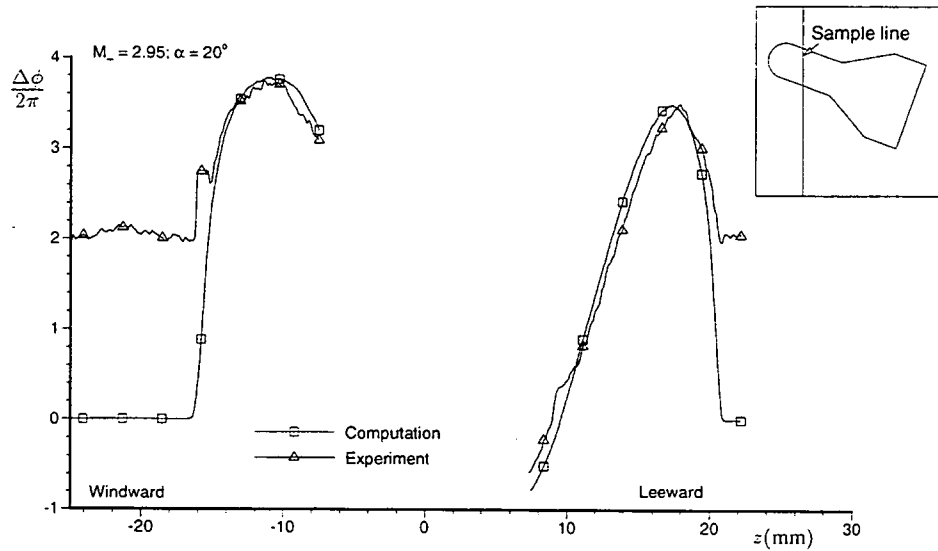


Figure 4.13: Unwrapped phase along vertical line, $M_\infty = 2.95$, $\alpha = 20^\circ$

respectively, in order to make a comparison with the numerical result. This shift is necessary, since the phase unwrapping in the experimental results fails at the shock due to the closely packed fringes. For the computations no phase unwrapping is necessary, since the phase angle $\Delta\phi$ is a direct result of the simulation process rather than the phase modulo 2π . The experimental and computational phase distribution agree rather well in the regions which are enclosed by the model and the shock. Comparison of the phase distribution in the flow outside of the shock shows that the phase period which has disappeared is 2π and 4π for $\alpha = 10^\circ$ and $\alpha = 20^\circ$, respectively.

4.3 Computations

The convergence history of the computations at $M_\infty = 2.95$ and $\alpha = 10^\circ$ and $\alpha = 20^\circ$ is given in Fig. 4.14. Figure 4.14(a) shows the logarithm (base 10) of the L_1 -norm of the residual as a function of the FAS-iteration number. The residual drops to engineering accuracy (10^{-4}) within 58 and 96 FAS iterations for $\alpha = 10^\circ$ and $\alpha = 20^\circ$ respectively. The lift- and drag coefficients, which do not include the forces on the base area, are obtained within 0.1% of its final value within 15 a 20 FAS-cycles, see Fig. 4.14(b).

Since viscous effects are not modelled by the Euler equations and the model is not equipped with sharp edges, the computational results do not predict separated flow. The bow-shock-wave topology is however predicted rather well by the numerical method. A three-dimensional view of the shock-wave pattern in the half space in the background is given in Fig. 4.15 for $M_\infty = 4.04$ and $\alpha = 20^\circ$. In this picture the shocks are represented as surfaces. These surfaces are calculated by an algorithm for the detection and visualization of shocks in a discrete flow field. The criterion used for the occurrence of a shock wave is that the velocity component in the direction of the local pressure gradient should pass the sonic value. Therefore the following scalar quantity is calculated:

$$M_{np} = \frac{1}{c} \mathbf{q} \cdot \frac{\nabla p}{\|\nabla p\|} \quad (4.1)$$

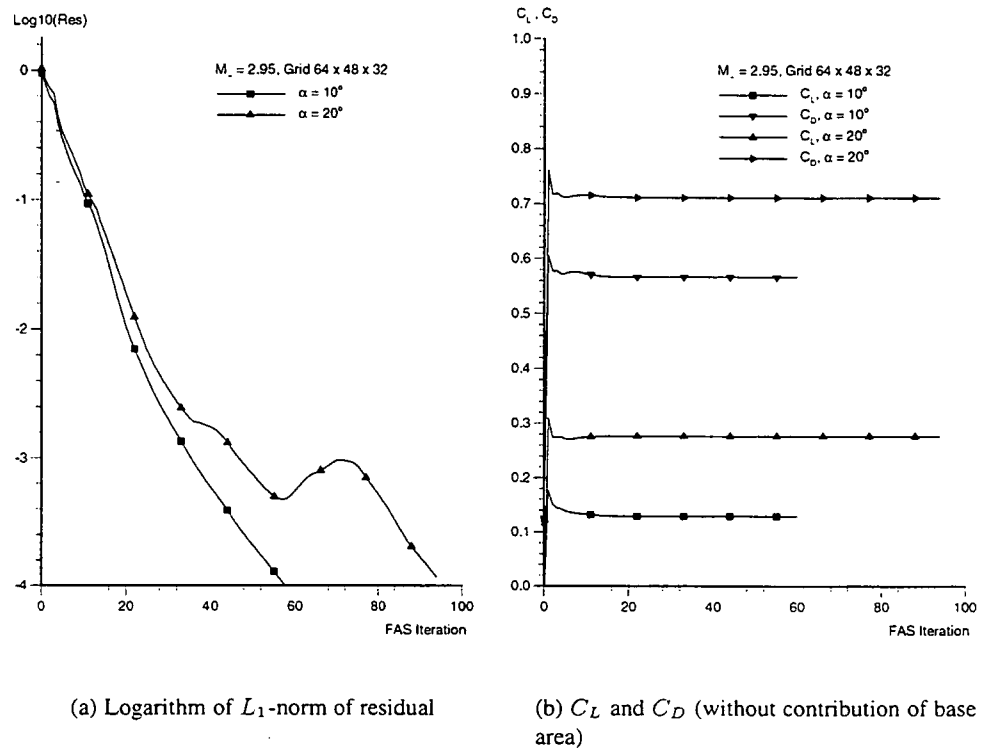


Figure 4.14: History of residual and aerodynamic forces, $M_\infty = 2.95$, $\alpha = 10^\circ$ and 20°

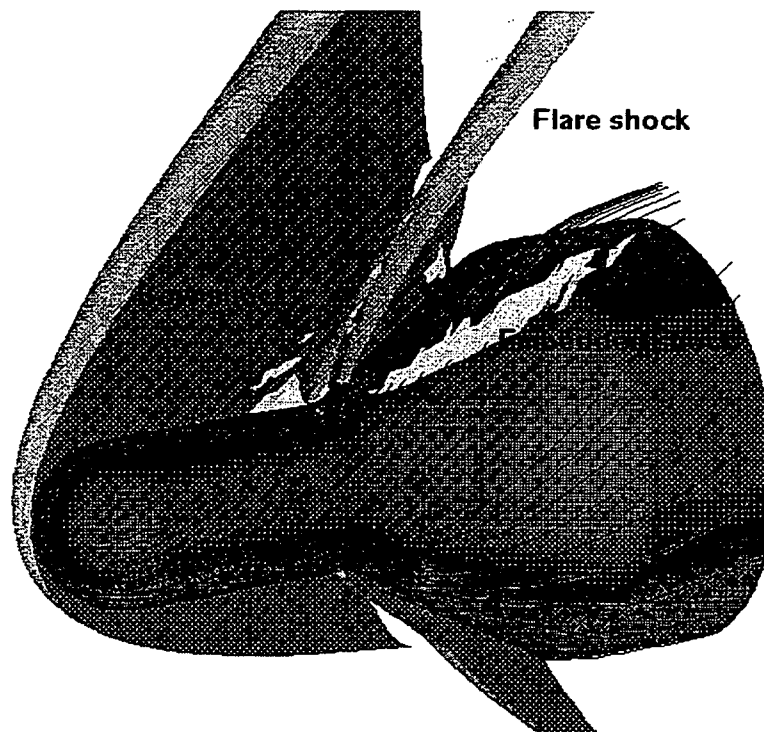


Figure 4.15: Shock pattern in computational data set, $M_\infty = 4.04$, $\alpha = 20^\circ$

where \mathbf{q} is the velocity vector, c the speed of sound and $\nabla p / \|\nabla p\|$ is the normalized pressure gradient. The shock surfaces are then represented as surfaces where $M_{np} = 1$, and the gradient of M_{np} along the local flow direction is negative ($\mathbf{q} \cdot \nabla M_{np} < 0$).

Besides the bow shock and the flare shock, this shock detection also reveals the existence of an embedded shock at the leeward side of the conical flare. Only this shock is also plotted in the foreground half-space. This shock can be filtered out of the isosurface by a selection criterion which uses the normal vectors of the triangular surfaces of the discrete shock surface. Only those triangles are plotted for which the angle between its normal vector and the assumed normal vector of the shock is less than a specified value. The position of this embedded shock corresponds with a curve at which the oil-streak lines show a kink (Figs.4.5,4.7).

Figure 4.16 shows the pressure distribution in the plane of symmetry for a calculation at $M_\infty = 4.04$ and $\alpha = 20^\circ$. The bow shock is captured within 2 cells in those regions where the shock is aligned with the grid (nose region). The isobars in the region between the shock-shock interaction and the model do not reveal an adjustment shock originating from the interaction point, which was observed in the shadowgraph and also follows from the heart-diagram analysis.

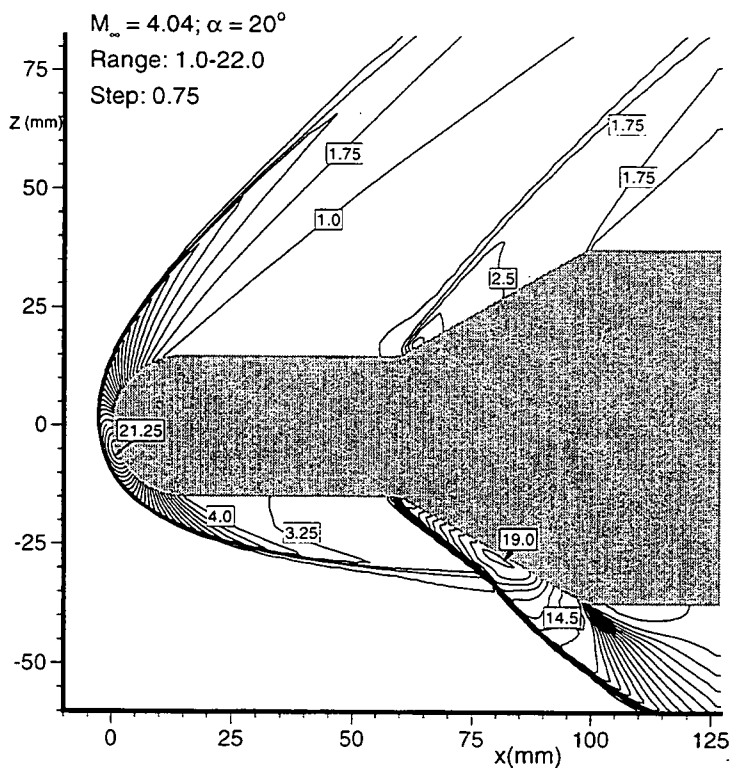


Figure 4.16: Isobars p/p_∞ in the plane of symmetry, $M_\infty = 4.04$, $\alpha = 20^\circ$

4.4 Surface pressure distributions

The surface pressure distributions obtained from the experiments and the computations at the windward- and leeward generator in the plane $y = 0$ are given in Figs. 4.17 - 4.20 for Mach numbers $M_\infty = 2.95$ and 4.04 and angles of attack $\alpha = 10^\circ$ and 20° . The pressure distributions from the computations agree very well with the experimental pressure distributions in those regions which are not dominated by viscosity effects, the windward sides of the hemispherical head and the cylinder. At the leeward side of the cylinder a separation causes a higher pressure than the computations (with attached flow) predict. Furthermore, differences occur at the beginning of the flare, where a shock-induced separation smears out the pressure increase in the experiments. At the leeward surface no shock can be observed in the experimental pressure distribution.

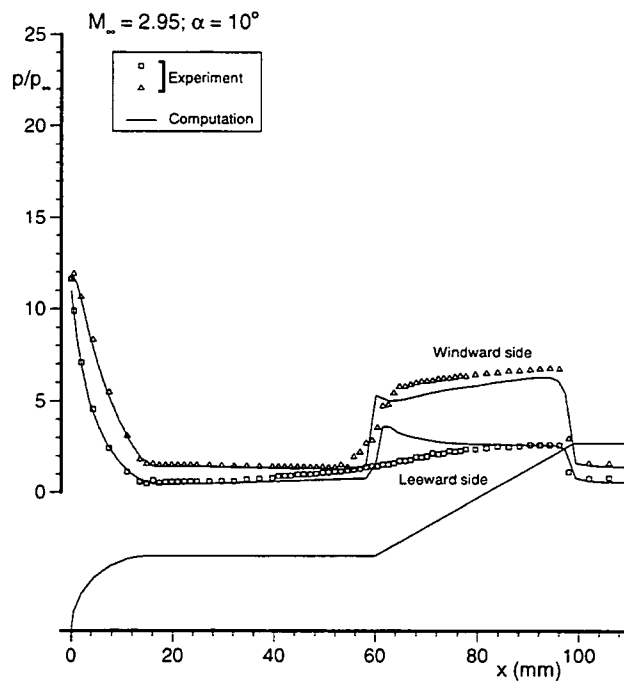


Figure 4.17: Computational and experimental surface pressure distribution at leeward- and windward generator, $M_\infty = 2.95$, $\alpha = 10^\circ$

For the lower angle of attack ($\alpha = 10^\circ$), the experimental and the computational pressure distributions at the flare agree rather well. In these cases the shock-shock interaction has no influence on the flare surface. Downstream of the flare, at the cylindrical part, the decrease of pressure due to the expansion is predicted rather well by the computational method for all angles of attack.

The effects of the shock-shock interaction on the pressure distribution at the windward side of the flare at $\alpha = 20^\circ$ are not predicted very well by the numerical simulations. In order to explain the behaviour of the pressure distribution at the windward side at $x > 80$ mm, the lines observed in the corresponding shadowgraphs are depicted in the Figures 4.18 and 4.20. They show that the lines coming from the interaction point, which are shocks according to the heart-diagram, coincide with a sudden increase of pressure on the surface. At $M_\infty = 4.04$ (Fig. 4.20) a significant expansion occurs just downstream of this shock, which coincides with another line coming from the interaction area and reflecting on the

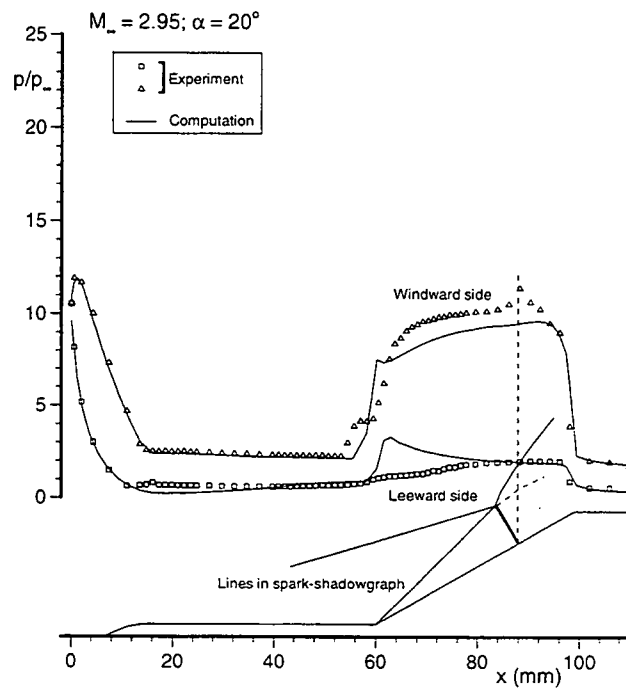


Figure 4.18: Computational and experimental surface pressure distribution at leeward- and windward generator, $M_\infty = 2.95$, $\alpha = 20^\circ$

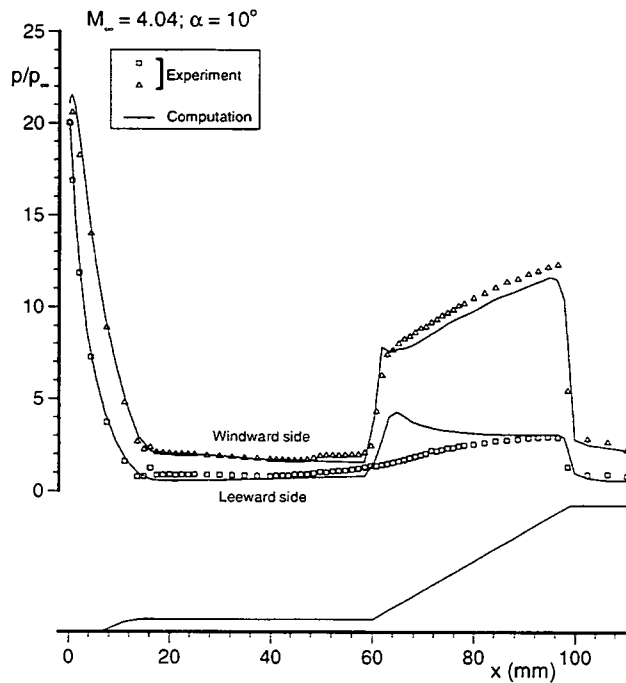


Figure 4.19: Computational and experimental surface pressure distribution at leeward- and windward generator, $M_\infty = 4.04$, $\alpha = 10^\circ$

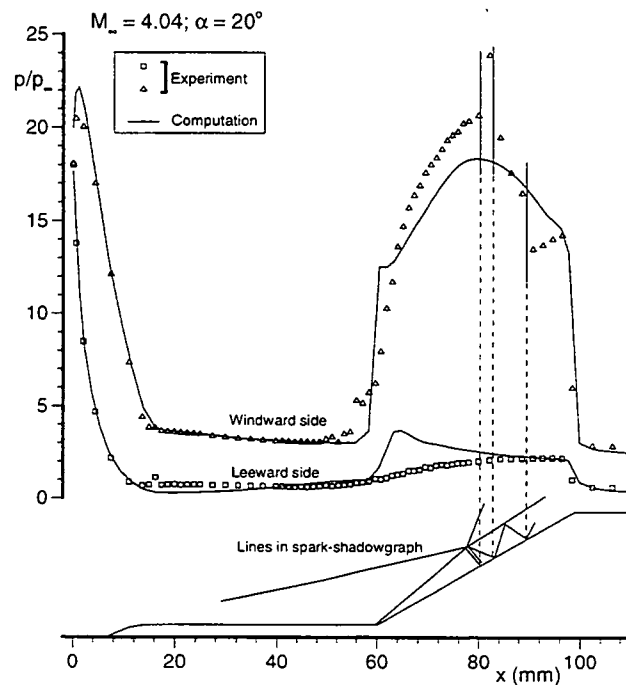


Figure 4.20: Computational and experimental surface pressure distribution at leeward- and windward generator, $M_\infty = 4.04$, $\alpha = 20^\circ$

surface. In the shadowgraph (Fig. 4.3) it is visible that this line reflects on the shear layer and again reflects on the surface, which coincides with another expansion.

The shock-shock interaction is an inviscid phenomenon, which should be modelled by the present numerical method. The weak adjustment shocks and expansion waves are not captured due to the numerical dissipation, which causes discontinuities to be smeared out when they are not aligned with grid lines. A finer grid in the x -direction (96 cells) with a clustering of points near the shock-shock interaction did not improve the result. The pressure distributions at the flare for the standard and the finer grid computations and the experiment are shown in Fig. 4.21.

The embedded shock at the flare, which was predicted by the shock detection algorithm, can also be observed in the computational leeward surface pressure distribution, which is given in the upper half of Fig. 4.22 together with some streamlines. The kink in the streamlines at this shock are also observed in the oil-flow visualization (Figs.4.5,4.7). The experimental pressure distribution, which is given in the lower half of Fig. 4.22, does not show the shock; apparently, the pressure rise through the shock is smeared out and decreased by the (turbulent) boundary layer. At the windward side the computational and experimental pressure distributions agree rather well at the cylindrical part (Fig. 4.23); at the flare the effect of the adjustment shock is not visible in the computational pressure distribution. The footprint of the adjustment shock in the experimental pressure distribution may be observed by the local maxima. The shape of this footprint is almost identical to the footprint observed in the oil-flow visualization (Fig. 4.6).

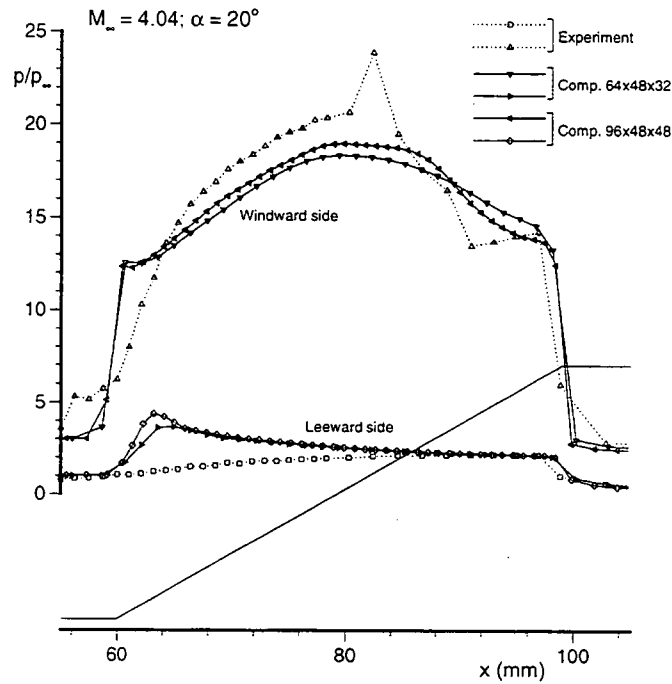


Figure 4.21: Computational and experimental surface pressure distribution at the leeward and windward generator of the flare, $M_\infty = 4.04$, $\alpha = 20^\circ$

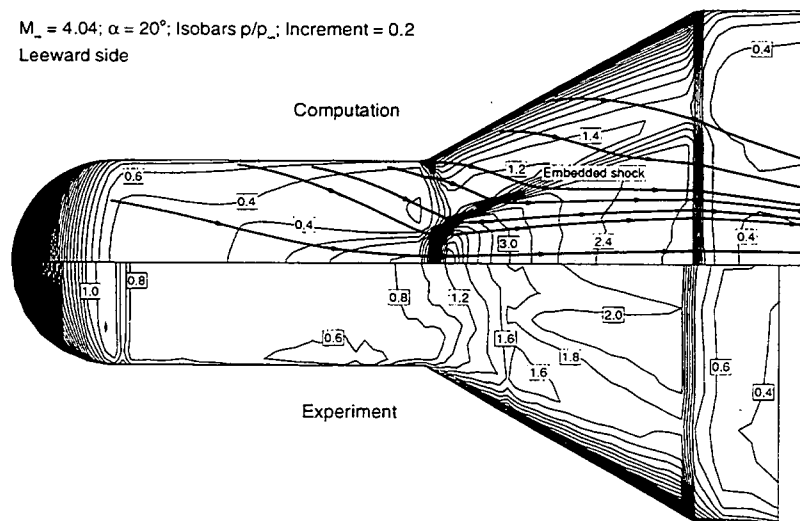


Figure 4.22: Computational and experimental leeward surface pressure distribution, $M_\infty = 4.04$, $\alpha = 20^\circ$

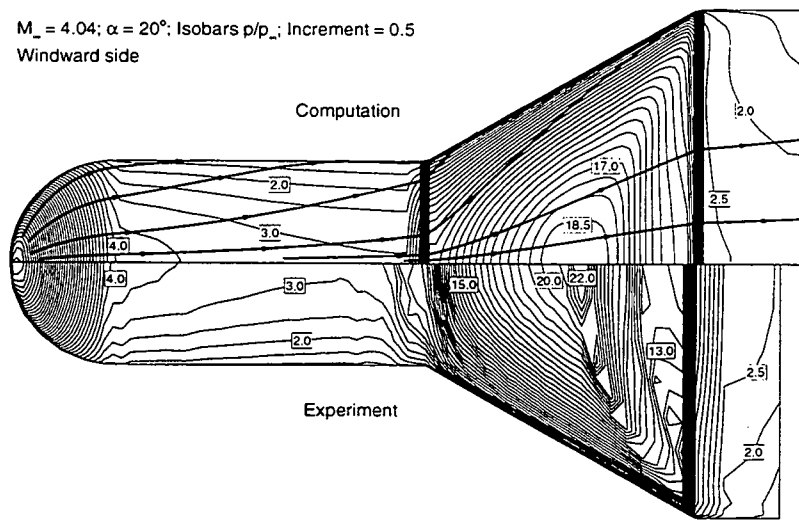


Figure 4.23: Computational and experimental windward surface pressure distribution,
 $M_\infty = 4.04$, $\alpha = 20^\circ$

Chapter 5

CONCLUSIONS

Different experimental techniques have been used to analyse the high-supersonic flow around a hemispherical-nose-cylinder with conical flare. The model has been investigated for flows with free-stream Mach numbers of 3 and 4 and angles of attack from 0° up to 20° . Interesting features of this flow are a complex surface flow topology, with various separations and their interactions, and a shock-shock interaction at large angles of attack in the windward region interfering with the body. The experiments are compared with computational results obtained from an Euler code.

Qualitative visualization techniques as spark shadowgraph and surface oil-flow appear to be a valuable tool to identify characteristic features about the flow topology and the shock patterns. High resolution surface pressure data support the interpretation of the visualization studies.

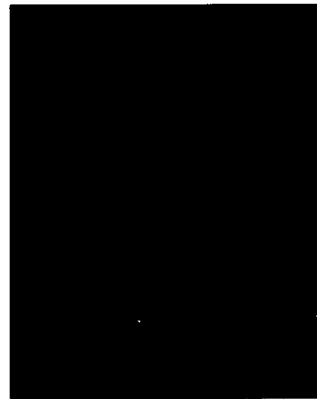
Digital Holographic Interferometry is a valuable tool for quantitative flow diagnostics, since the entire integrated density field is captured at a single moment. It may serve as a validation instrument for computer codes, because the integrated density can be compared directly to post-processed numerical results. Difficult areas in the flow field are areas with high density gradients (shock waves) normal to the light rays, where the phase-unwrapping process fails. Simulated phase maps were obtained from discrete solutions of a 3D Euler code, neglecting the light ray deflection. The experimental results and the post-processed Euler results show a rather good agreement in those areas which are not affected by viscous effects or by shock waves. Comparing interferometric and numerical results can serve multiple purposes, as differences may reveal flaws in both methods and can assist in mutual interpretation of the results. Comparison of both phase maps gives some insight into the possible causes for "bad" points in the interferometric results. E.g., the Euler code results reveal that the areas indicated as unreliable in the interferometry (because of low modulation intensity) near the shock waves and expansion areas at the flare-cylinder junction are caused by a strong density gradient, so that the sampling condition cannot be met.

The computational results are compared with detailed surface pressure measurements. The pressure distribution at the nose and the windward side of the model is predicted rather well by the Euler code. At the leeward side, where the flow is dominated by the presence of separation and vortex formation, the agreement between experimental pressure and computational pressures is rather poor, as may be expected. The surface pressure distributions at 20° angle of attack indicate adjustment shocks and expansion waves originating from the shock-shock interaction in the windward flow field. The adjustment shock- and expansion waves, which interfere with the body, are however not captured by the numerical method due to numerical dissipation. In order to capture these phenomena, a very fine grid in the shock-shock interaction region should be used.

REFERENCES

- ANDERSON, W.K., THOMAS, J.L., AND WHITFIELD, D.L. (1988) "Multigrid Acceleration of the Flux-split Euler Equations," *AIAA Journal*, **26**(6):649–654.
- BAKKER, P.G. AND BANNINK, W.J. (1992) "Experimental Visualization of Viscous Interaction Effects in Compressible Flow Field," Annual report 1992, pp. 18–28, J.M. Burgers Centre for Fluid Mechanics.
- BAKKER, P.G., BANNINK, W.J., AND LUSSE, P.A. (1992) "Experimental Investigation of the High Supersonic Flowfield past a Re-entry Body," In Brun, R. and Chikhaoui, A.A., editors, *IUTAM Symposium: Aerothermochemistry of Spacecrafts and Associated Hypersonic Flows*, pp. 413–418, Marseille.
- BANNINK, W.J. (1963) "De verdeling van het getal van Mach bij een beperkt gedeelte van de meetplaats van de supersonische wind tunnel no. 2 bij een nominaal getal van Mach van 3," Memorandum m-75, Dept. of Aerospace Engineering, Delft University of Technology.
- EDNEY, B. (1968) "Anomalous Heat Transfer and Pressure Distributions on Blunt Bodies at Hypersonic Speeds in the Presence of an Impinging Shock," FFA Report 115, The Aeronautical Research Institute of Sweden.
- FRANÇON, M. (1974) "*Holography*," Academic Press, New York.
- HEMKER, P.W. AND KOREN, B. (1995) "Defect Correction and Nonlinear Multigrid for the Steady Euler Equations," In Habashi, W.G. and Hafez, M.M., editors, *Computational Fluid Dynamics Techniques*, pp. 699 – 718. Gordon and Breach, Basel.
- LANEN, T.A.W.M. (1992) "*Digital Holographic Interferometry in Compressible Flow Research*," PhD thesis, Delft University of Technology.
- LANEN, T.A.W.M., BAKKER, P.G., AND BRYANSTON-CROSS, P.J. (1992) "Digital Holographic Interferometry in High-Speed Flow Research," *Experiments in Fluids*, **13**:56–62.
- LANEN, T. AND HOUTMAN, E.M. (1992) "Comparison of Interferometric Measurements with 3-D Euler Computations for Circular Cones in Supersonic Flow," AIAA Paper 92-2691 CP.
- LANEN, T.A.W.M., NEBBELING, C., AND INGEN, J.L. VAN (1990) "Phase-stepping Holographic Interferometry in Studying Transparent Density Fields around 2-D Objects of Arbitrary Shape," *Opt. Comm.*, **76**:268–276.
- LEER, B. VAN (1977) "Towards the Ultimate Conservation Difference Scheme IV; A New Approach to Numerical Convection," *Journal of Comp. Physics*, **23**:276–299.
- LEER, B. VAN (1982) "Flux-Vector Splitting for the Euler Equations," *Lecture Notes in Physics*, **170**:507–512.
- LUSSE, P. (1992) "Visualisation Study of a Blunt-Cylinder-Flare Model in High Supersonic Flow," Graduate thesis, Dept. of Aerospace Engineering, Delft University of Technology.

- MONTGOMERY, G.P. AND REUSS, D.L. (1982) "Effects of Refraction on Axisymmetric Flame Temperatures measured by Holographic Interferometry," *Appl. Opt.*, **21**:1373–1380.
- OSHER, S. AND SOLOMON, F. (1982) "Upwind Difference Schemes for Hyperbolic Systems of Conservation Laws," *Math. Comp.*, **38**:339–374.
- REGINATO, S. (1993) "Pressure Measurements on a Blunt-Cylinder-Flare Model in High Supersonic Flow," Graduate thesis, Delft University of Technology/ University of Pisa.
- ROE, P.L. (1981) "Approximate Riemann Solvers, Parameter Vectors and Difference Schemes," *Journal of Comp. Physics*, **43**:357–372.
- SPEKREIJSE, S.P. (1987) "*Multigrid Solution of the Steady Euler Equations*," PhD thesis, Delft University of Technology.



01/23/2024 10:08:11 AM

Rapport 796



60141010237

960274